INFORMATION TO USERS

This reproduction was made from a copy of a document sent to us for microfilming. While the most advanced technology has been used to photograph and reproduce this document, the quality of the reproduction is heavily dependent upon the quality of the material submitted.

The following explanation of techniques is provided to help clarify markings or notations which may appear on this reproduction.

1. The sign or "target" for pages apparently lacking from the document photographed is "Missing Page(s)". If it was possible to obtain the missing page(s) or section, they are spliced into the film along with adjacent pages. This may have necessitated cutting through an image and duplicating adjacent pages to assure complete continuity.

2. When an image on the film is obliterated with a round black mark, it is an indication of either blurred copy because of movement during exposure, duplicate copy, or copyrighted materials that should not have been filmed. For blurred pages, a good image of the page can be found in the adjacent frame. If copyrighted materials were deleted, a target note will appear listing the pages in the adjacent frame.

3. When a map, drawing or chart, etc., is part of the material being photographed, a definite method of "sectioning" the material has been followed. It is customary to begin filming at the upper left hand corner of a large sheet and to continue from left to right in equal sections with small overlaps. If necessary, sectioning is continued again—beginning below the first row and continuing on until complete.

4. For illustrations that cannot be satisfactorily reproduced by xerographic means, photographic prints can be purchased at additional cost and inserted into your xerographic copy. These prints are available upon request from the Dissertations Customer Services Department.

5. Some pages in any document may have indistinct print. In all cases the best available copy has been filmed.

University
Microfilms
International

300 N. Zeeb Road
Ann Arbor, MI 48106

8307796

Venkatapathy, Ethiraj

A GENERALIZED SOLUTION TECHNIQUE FOR THE PARABOLIZED
NAVIER-STOKES EQUATIONS

Iowa State University   .   PH.D.   1982

University
Microfilms
International   300 N. Zeeb Road, Ann Arbor, MI 48106

A generalized solution technique for the

parabolized Navier-Stokes equations

by

Ethiraj Venkatapathy

A Dissertation Submitted to the

Graduate Faculty in Partial Fulfillment of the

Requirements for the Degree of

DOCTOR OF PHILOSOPHY

Major: Aerospace Engineering

Approved:

In Charge of Major Work

For the Major Department

For the Graduate 'College

Iowa State University
Ames, Iowa

1982

TABLE OF CONTENTS

I. INTRODUCTION

The parabolized Navier-Stokes (PNS) equations are a subset of the full steady Navier-Stokes equations. A large class of steady supersonic high-Reynolds-number viscous flows about arbitrary configurations can be solved efficiently by using the PNS equations. In order to apply the PNS equations, the inviscid region of the flow field must be supersonic and the streamwise velocity component must not be negative (i.e., only cross flow separation is permitted). If these conditions are met, the PNS equations can be used to compute the flow field at a fraction of the computer cost required to solve the complete time-dependent Navier-Stokes equations. In addition, viscous-inviscid interaction problems which have plagued boundary layer methods are eliminated with the PNS equations. Computational efficiency and reduced storage requirements are achieved because the PNS equations are solved by advancing a two-dimensional array of data in space, rather than advancing a three-dimensional array of data in time, as is done for the full Navier-Stokes equations.

Rubin and Lin (1), Lin and Rubin (2) and Lubard and Helliwell (3) were the first to use the PNS equations to calculate the viscous supersonic flow around bodies at angles of incidence. Later, viscous flow around blunt nose bodies (4, 5) were calculated. Though the earlier methods were successful, poor reliability and efficiency led to the search for more efficient and stable schemes, resulting in fully implicit noniterative marching schemes, first due to Vigneron et al. (6) and later Schiff and Steger (7). These methods were limited by marching planes that are

normal to the marching axis, and their applications were confined to conical and axisymmetric body shapes. In the present study, a generalized PNS solution procedure is presented. This procedure (8) couples the efficiency and stability of the numerical technique developed by Vigneron et al. (6) with a generalized marching technique.

The calculation of the complete inviscid-viscous flow around the Space Shuttle Orbiter with a single code has been the aim of recent research efforts. Although the inviscid flow solutions (9-14) and other solution techniques that couple the inviscid solutions with the matching boundary layer analysis (15, 16) have resulted in limited solutions for the windward side of Shuttle-like bodies, they have failed in general to predict the correct solution on the lee side and near the wing root region. On the other hand, PNS solvers have shown great promise in solving the complex flow field around Shuttle-like bodies (17, 18). Recently, C. P. Li (17) obtained the windward and lee side viscous-inviscid solution for a Shuttle-like configuration and Chaussee et al. (18) were able to obtain solutions around the X-24C aircraft configuration. In both of these cases, the flow field development near the wing body juncture and the wing tip were not studied due to the geometric complexity.

The present generalized PNS solver, on the other hand, adapts well to the complex flow that develops around leading edges and in the vicinity of wing body junctures. Two complex flow problems are considered here. The first problem involves calculating the laminar flow over a slab delta wing with 70° sweep at angles of attack up to 41.5° and Mach numbers of 6.8 and 9.6. The full capabilities of the generalized

marching procedure are used in the second problem where the laminar flow around the Space Shuttle Orbiter forebody region at angles of attack of 0° and 30°, and Mach numbers of 4.6 and 7.9, respectively, are computed. An algebraic grid generation scheme used in this study, clusters the grid points and accurately describes the body shape. The computed results for both problems are compared with available experimental results.

II.   PARABOLIZED NAVIER-STOKES EQUATIONS

IN GENERALIZED COORDINATES

The Navier-Stokes equations for an unsteady three-dimensional flow without body forces or external heat addition can be written in nondimensional, conservation-law form for a Cartesian coordinate system as

$$\frac{\partial U}{\partial t} + \frac{\partial (E-E_v)}{\partial x} + \frac{\partial (F-F_v)}{\partial y} + \frac{\partial (G-G_v)}{\partial z} = 0 \qquad (1)$$

where

$$U = \begin{bmatrix} \rho \\ \rho u \\ \rho v \\ \rho w \\ \rho e_t \end{bmatrix} \qquad (2)$$

$$E = \begin{bmatrix} \rho u \\ \rho u^2 + p \\ \rho uv \\ \rho uw \\ (\rho e_t + p)u \end{bmatrix} \qquad E_v = \begin{bmatrix} 0 \\ \sigma_{xx} \\ \tau_{xy} \\ \tau_{xz} \\ u\sigma_{xx} + v\tau_{xy} + w\tau_{xz} + q_x \end{bmatrix} \qquad (3)$$

$$F = \begin{bmatrix} \rho v \\ \rho uv \\ \rho v^2 + p \\ \rho vw \\ (\rho e_t + p)v \end{bmatrix} \qquad F_V = \begin{bmatrix} 0 \\ \tau_{xy} \\ \sigma_{yy} \\ \tau_{yz} \\ u\tau_{xy}+v\sigma_{yy}+w\tau_{yz}+q_y \end{bmatrix} \qquad (4)$$

$$G = \begin{bmatrix} \rho w \\ \rho uw \\ \rho vw \\ \rho w^2 + p \\ (\rho e_t + p)w \end{bmatrix} \qquad G_V = \begin{bmatrix} 0 \\ \tau_{xz} \\ \tau_{yz} \\ \sigma_{zz} \\ u\tau_{xz}+v\tau_{yz}+w\sigma_{zz}+q_z \end{bmatrix} \qquad (5)$$

$$e_t = e + \frac{u^2 + v^2 + w^2}{2} \qquad (6)$$

and

$$\sigma_{xx} = \frac{2\mu}{3Re_L}\left(2\frac{\partial u}{\partial x} - \frac{\partial v}{\partial y} - \frac{\partial w}{\partial z} \right)$$

$$\sigma_{yy} = \frac{2\mu}{3Re_L}\left(2\frac{\partial v}{\partial y} - \frac{\partial u}{\partial x} - \frac{\partial w}{\partial z} \right)$$

$$\sigma_{zz} = \frac{2\mu}{3Re_L}\left(2\frac{\partial w}{\partial z} - \frac{\partial u}{\partial x} - \frac{\partial v}{\partial y} \right)$$

$$\tau_{xy} = \frac{\mu}{Re_L}\left(\frac{\partial u}{\partial y} + \frac{\partial v}{\partial x}\right)$$

$$\tau_{xz} = \frac{\mu}{Re_L}\left(\frac{\partial u}{\partial z} + \frac{\partial w}{\partial x}\right)$$

$$\tau_{yz} = \frac{\mu}{Re_L}\left(\frac{\partial v}{\partial z} + \frac{\partial w}{\partial y}\right)$$

(7)

$$q_x = \frac{\mu}{(\gamma - 1)M_\infty^2 Re_L Pr}\frac{\partial T}{\partial x}$$

$$q_y = \frac{\mu}{(\gamma - 1)M_\infty^2 Re_L Pr}\frac{\partial T}{\partial y}$$

$$q_z = \frac{\mu}{(\gamma - 1)M_\infty^2 Re_L Pr}\frac{\partial T}{\partial z}$$

These equations have been nondimensionalized as follows (dimensional quantities are denoted by a tilde)

$$x = \frac{\tilde{x}}{\tilde{L}} \qquad y = \frac{\tilde{y}}{\tilde{L}} \qquad z = \frac{\tilde{z}}{\tilde{L}} \qquad t = \frac{\tilde{t}}{\tilde{L}/\tilde{V}_\infty}$$

$$u = \frac{\tilde{u}}{\tilde{V}_\infty} \qquad v = \frac{\tilde{v}}{\tilde{V}_\infty} \qquad w = \frac{\tilde{w}}{\tilde{V}_\infty} \qquad e = \frac{\tilde{e}}{\tilde{V}_\infty^2} \qquad (8)$$

$$\rho = \frac{\tilde{\rho}}{\tilde{\rho}_\infty} \qquad p = \frac{\tilde{p}}{\tilde{\rho}_\infty \tilde{V}_\infty^2} \qquad T = \frac{\tilde{T}}{\tilde{T}_\infty} \qquad \mu = \frac{\tilde{\mu}}{\tilde{\mu}_\infty}$$

where $\tilde{L}$ is the reference length used in the Reynolds number

$$Re_L = \frac{\tilde{\rho}_\infty \tilde{V}_\infty \tilde{L}}{\tilde{\mu}_\infty} \qquad (9)$$

In order to close the system of equations, the following perfect gas equations of state are used

$$p = (\gamma - 1)\rho e$$

$$T = \gamma M_\infty^2 \, p/\rho \tag{10}$$

and the coefficient of viscosity (μ) is determined from Sutherland's equation

$$\mu = T^{3/2} \left(\frac{1 + C}{T + C}\right) \tag{11}$$

where C equals 110.4 $K/\tilde{T}_\infty$ for air. In the original study of Vigneron et al. (6), the following transformation was used

$$\xi = \xi(x)$$

$$\eta = \eta(x,y,z) \tag{12}$$

$$\zeta = \zeta(x,y,z)$$

This transformation restricts the (η,ζ) solution surfaces to be in a plane normal to the x axis and thereby limits the flowfields which can be computed with the code. In the present study, a completely general transformation of the form

$$\xi = \xi(x,y,z)$$

$$\eta = \eta(x,y,z) \tag{13}$$

$$\zeta = \zeta(x,y,z)$$

is used which places no restrictions on the orientation of the (η,ζ) solution surfaces. When this transformation is applied to Eq. (1), the following conservation-law form (19) is obtained

$$\frac{\partial \bar{U}}{\partial t} + \frac{\partial}{\partial \xi}\left\{\frac{1}{J}\left[\xi_x(E-E_v) + \xi_y(F-F_v) + \xi_z(G-G_v)\right]\right\}$$

$$+ \frac{\partial}{\partial \eta}\left\{\frac{1}{J}\left[\eta_x(E-E_v) + \eta_y(F-F_v) + \eta_z(G-G_v)\right]\right\}$$

$$+ \frac{\partial}{\partial \zeta}\left\{\frac{1}{J}\left[\zeta_x(E-E_v) + \zeta_y(F-F_v) + \zeta_z(G-G_v)\right]\right\} = 0 \qquad (14)$$

where

$$\bar{U} = U/J \qquad (15)$$

and J is the Jacobian of the transformation which can be evaluated from

$$J = 1\Big/\left[x_\xi(y_\eta z_\zeta - y_\zeta z_\eta) - x_\eta(y_\xi z_\zeta - y_\zeta z_\xi) + x_\zeta(y_\xi z_\eta - y_\eta z_\xi)\right] \qquad (16)$$

The metrics are given by the expressions

$$\xi_x = J(y_\eta z_\zeta - y_\zeta z_\eta)$$

$$\xi_y = -J(x_\eta z_\zeta - x_\zeta z_\eta)$$

$$\xi_z = J(x_\eta y_\zeta - x_\zeta y_\eta)$$

$$\eta_x = -J(y_\xi z_\zeta - y_\zeta z_\xi)$$

$$\eta_y = J(x_\xi z_\zeta - x_\zeta z_\xi) \qquad (17)$$

$$\eta_z = -J(x_\xi y_\zeta - x_\zeta y_\xi)$$

$$\zeta_x = J(y_\xi z_\eta - y_\eta z_\xi)$$

$$\zeta_y = -J(x_\xi z_\eta - x_\eta z_\xi)$$

$$\zeta_z = J(x_\xi y_\eta - x_\eta y_\xi)$$

and the partial derivatives appearing in the viscous terms E_v, F_v, G_v are transformed with the aid of the equations

$$\frac{\partial}{\partial x} = \xi_x \frac{\partial}{\partial \xi} + \eta_x \frac{\partial}{\partial \eta} + \zeta_x \frac{\partial}{\partial \zeta}$$

$$\frac{\partial}{\partial y} = \xi_y \frac{\partial}{\partial \xi} + \eta_y \frac{\partial}{\partial \eta} + \zeta_y \frac{\partial}{\partial \zeta} \tag{18}$$

$$\frac{\partial}{\partial z} = \xi_z \frac{\partial}{\partial \xi} + \eta_z \frac{\partial}{\partial \eta} + \zeta_z \frac{\partial}{\partial \zeta}$$

The "parabolized" Navier-Stokes equations are derived from the complete Navier-Stokes equations by assuming:

1) Steady flow $\left(\frac{\partial}{\partial t} \equiv 0\right)$

2) Streamwise viscous derivatives are negligible compared to normal and circumferential viscous derivatives $\left(\frac{\partial}{\partial \xi}[\text{viscous terms}] \cong 0\right)$

With these assumptions, Eq. (14) reduces to

$$\frac{\partial \bar{E}}{\partial \xi} + \frac{\partial \bar{F}}{\partial \eta} + \frac{\partial \bar{G}}{\partial \zeta} = 0 \tag{19}$$

where

$$\bar{E} = \frac{1}{J}(\xi_x E + \xi_y F + \xi_z G)$$

$$\bar{F} = \frac{1}{J}\left[\eta_x(E-E_v) + \eta_y(F-F_v) + \eta_z(G-G_v)\right] \tag{20}$$

$$\bar{G} = \frac{1}{J}\left[\zeta_x(E-E_v) + \zeta_y(F-F_v) + \zeta_z(G-G_v)\right]$$

and terms in E_v, F_v, and G_v containing partial derivatives with respect to ξ are omitted.

As mentioned previously, the above system of equations is "parabolized" in the ξ direction if the inviscid region of the flow is supersonic and if the streamwise velocity component is positive. However, it has been shown (20) that an exact representation of the streamwise pressure gradient term, $\partial p/\partial \xi$, causes information to be propagated upstream through the subsonic boundary layer close to the wall so that a marching method of solution is not well-posed. This leads to exponentially growing solutions which are often called departure solutions. A number of different techniques have been proposed to eliminate this difficulty. Lin and Rubin (21) recently compared these techniques while proposing a new one. The obvious technique is to drop completely the pressure gradient term in subsonic regions. This will produce a stable marching scheme but will introduce errors in flowfields with large streamwise pressure gradients. In several studies (2, 3, 4, 5, 22, 23), $\partial p/\partial \xi$ is retained in the subsonic layer by employing an approximate backward difference formula which can be extrapolated from the previous step. The eigenvalue stability analyses of Refs. 3 and 6 indicate this approach is subject to instabilities if the streamwise step $\Delta \xi$ is too small. Rubin and Lin (1) originally proposed the so-called "sublayer approximation" technique in which the pressure gradient term in the subsonic region is calculated at a supersonic point outside the sublayer region. This approximation is based on the fact that for a thin subsonic viscous layer, $\partial p/\partial \eta$ is negligible. The "sublayer approximation" technique is used in the code of Schiff and Steger (7). Note, however, that the method originally employed by Rubin and Lin is essentially different in that the boundary layer equations were solved in the sublayer.

Schiff and Steger's "sublayer approximation" technique is explained further after the next paragraph.

A novel technique for handling the pressure gradient term was proposed by Vigneron et al. (6). In this approach, a fraction of the pressure gradient term $\omega(\partial p/\partial \xi)$ is retained in the subsonic viscous region and the remainder $(1-\omega)\partial p/\partial \xi$ is separated out and evaluated outside the subsonic region as in the "sublayer approximation" technique. An eigenvalue stability analysis indicates that for stability

$$\omega < \frac{\gamma M_\xi^2}{1 + (\gamma-1)M_\xi^2} \qquad (21)$$

where M_ξ is the local streamwise Mach number. For certain cases, the retention of the term, $(1-\omega)\partial p/\partial \xi$, will lead to departure solutions. In the present study, this difficulty was encountered only at very high angles of attack and in these cases, the term was simply dropped.

The "sublayer approximation" method of Schiff and Steger utilizes the following step function in place of Eq. (21)

$$\omega = \begin{cases} 1 \text{ if } M_\xi > M* \\ \\ 0 \text{ if } M_\xi \leq M* \end{cases}$$

where M* is a specified value near 1. Their method also removes the streamwise pressure gradient term from the energy equation in the sublayer region. To avoid departure solutions, Schiff and Steger (7) suggest using a global iteration procedure.

In order to facilitate the application of the "Vigneron" technique, Eq. (19) is rewritten as

$$\frac{\partial \bar{E}*}{\partial \xi} + \frac{\partial \bar{P}}{\partial \xi} + \frac{\partial \bar{F}}{\partial \eta} + \frac{\partial \bar{G}}{\partial \zeta} = 0 \qquad\qquad (22)$$

where

$$\bar{E} = \bar{E}* + \bar{P} \qquad\qquad (23)$$

and

$$\bar{E}* = \frac{1}{J}\left(\xi_x E* + \xi_y F* + \xi_z G*\right)$$

$$\bar{P} = \frac{1}{J}\left(\xi_x P_1 + \xi_y P_2 + \xi_z P_3\right)$$

$$E* = E - P_1$$

$$F* = F - P_2$$

$$G* = G - P_3$$

$$P_1 = [0,(1-\omega)p,0,0,0]^T \qquad\qquad (24)$$

$$P_2 = [0,0,(1-\omega)p,0,0]^T$$

$$P_3 = [0,0,0,(1-\omega)p,0]^T$$

The generalized PNS code has been programmed to give the user the option of specifying either the "Vigneron" technique or the "sublayer approximation" technique of handling the streamwise pressure gradient term in the momentum equations.

III. FINITE DIFFERENCE ALGORITHM

Until recently, the PNS equations have been solved using iterative, implicit, finite-difference schemes. Vigneron et al. (6) were the first to employ a more efficient noniterative, implicit, approximate-factored, finite-difference scheme to solve the PNS equations. This algorithm is a direct descendant of the schemes developed by Lindemuth and Killeen (24), McDonald and Briley (25), and Beam and Warming (26) to initially solve the unsteady Navier-Stokes equations.

The detailed development of the implicit, noniterative, approximate-factored scheme, as applied to the PNS equations in generalized co-ordinates, is given in Appendix A. The resulting delta form of the algorithm is

$$
\left[\frac{\partial \bar{\bar{E}}^*}{\partial \bar{U}} + \frac{\theta_1}{1+\theta_2} \Delta\xi \frac{\partial}{\partial\zeta}\left(\frac{\partial \bar{G}}{\partial \bar{U}}\right)\right] \left(\frac{\partial \bar{\bar{E}}^*}{\partial \bar{U}}\right)^{-1} \left[\frac{\partial \bar{\bar{E}}^*}{\partial \bar{U}} + \frac{\theta_1}{1+\theta_2} \Delta\xi \frac{\partial}{\partial\eta}\left(\frac{\partial \bar{F}}{\partial \bar{U}}\right)\right] \Delta^i\bar{U}
$$

$$
= \frac{-\Delta\xi}{1+\theta_2}\left(\frac{\partial \bar{F}}{\partial\eta} + \frac{\partial \bar{G}}{\partial\zeta}\right)^i + \frac{\theta_2}{1+\theta_2}\Delta^{i-1}\bar{E} - \Delta^i\bar{P}
$$

$$
- \Delta\xi\left(\frac{\partial \bar{\bar{E}}^*}{\partial\xi}\right)^i_{\bar{U}} - \frac{\theta_1}{1+\theta_2}(\Delta\xi)^2\left[\frac{\partial}{\partial\eta}\left(\frac{\partial \bar{F}}{\partial\xi}\right)^i_{\bar{U}} + \frac{\partial}{\partial\zeta}\left(\frac{\partial \bar{G}}{\partial\xi}\right)^i_{\bar{U}}\right] \qquad (25)
$$

where subscript i refers to the station $\xi = i\Delta\xi$ and

$$
\Delta^i\bar{U} = \bar{U}^{i+1} - \bar{U}^i \qquad (26)
$$

The terms $\left(\frac{\partial \bar{\bar{E}}^*}{\partial\xi}\right)^i_{\bar{U}}$, $\left(\frac{\partial \bar{F}}{\partial\xi}\right)^i_{\bar{U}}$, and $\left(\frac{\partial \bar{G}}{\partial\xi}\right)^i_{\bar{U}}$ are evaluated with the aid of the expressions

$$
\left(\frac{\partial \bar{\bar{E}}^*}{\partial\xi}\right)_{\bar{U}} = \left(\frac{E^*}{J}\right)\frac{\partial \xi_x}{\partial\xi} + \left(\frac{F^*}{J}\right)\frac{\partial \xi_y}{\partial\xi} + \left(\frac{G^*}{J}\right)\frac{\partial \xi_z}{\partial\xi}
$$

$$\left(\frac{\partial \bar{F}}{\partial \xi}\right)_{\bar{U}} = \left(\frac{E-E_v}{J}\right)\frac{\partial \eta_x}{\partial \xi} + \left(\frac{F-F_v}{J}\right)\frac{\partial \eta_y}{\partial \xi} + \left(\frac{G-G_v}{J}\right)\frac{\partial \eta_z}{\partial \xi}$$

$$\left(\frac{\partial \bar{G}}{\partial \xi}\right)_{\bar{U}} = \left(\frac{E-E_v}{J}\right)\frac{\partial \zeta_x}{\partial \xi} + \left(\frac{F-F_v}{J}\right)\frac{\partial \zeta_y}{\partial \xi} + \left(\frac{G-G_v}{J}\right)\frac{\partial \zeta_z}{\partial \xi} \qquad (27)$$

where $\left(\quad\right)_{\bar{U}}$ indicates $\bar{U}$ is held constant. The Jacobians $\partial \bar{F}/\partial \bar{U}$, $\partial \bar{G}/\partial \bar{U}$ and $\partial \bar{E}*/\partial \bar{U}$ are given in Appendix B. The partial derivatives $\partial/\partial \eta$ and $\partial/\partial \zeta$ are approximated by second-order accurate central differences.

For first-order accuracy in ξ, the Euler implicit scheme $(\theta_1 = 1, \theta_2 = 0)$ is used. In this case, the Jacobians are evaluated at station i and the last term in brackets in Eq. (25) is dropped. Also, the explicit stream-wise pressure gradient term $\Delta^1 \bar{P}$ (which appears only in the sublayer region) is evaluated at a point outside the sublayer region using a first-order backward difference at station i. All of the results presented here were obtained with the Euler implicit scheme.

If second-order accuracy in ξ is desired, the three-point backward implicit scheme $(\theta_1 = 1, \theta_2 = 1/2)$ can be used. In this case, the Jacobians are evaluated at i+1/2 and the explicit streamwise pressure gradient term is evaluated at a point outside the sublayer region using a second-order backward difference at station i.

The algorithm given by Eq. (25) is implemented in the following manner:

Step 1

$$\left[\frac{\partial \bar{E}*}{\partial \bar{U}} + \frac{\theta_1}{1+\theta_2} \Delta \xi \frac{\partial}{\partial \zeta}\left(\frac{\partial \bar{G}}{\partial \bar{U}}\right)\right]\Delta \bar{U}_1 = RHS[Eq. 27] \qquad (28a)$$

Step 2

$$\Delta \bar{U}_2 = \frac{\partial \bar{\bar{E}}^*}{\partial \bar{\bar{U}}} \; \Delta \bar{U}_1 \qquad (28b)$$

Step 3

$$\left[\frac{\partial \bar{\bar{E}}^*}{\partial \bar{\bar{U}}} + \frac{\theta_1}{1+\theta_2} \; \Delta\xi \; \frac{\partial}{\partial \eta}\left(\frac{\partial \bar{\bar{F}}}{\partial \bar{\bar{U}}} \right) \right] \Delta^i \bar{U} = \Delta \bar{U}_2 \qquad (28c)$$

Step 4

$$\bar{U}^{i+1} = \bar{U}^i + \Delta^i \bar{U} \qquad (28d)$$

In Eq. (28a), $\Delta \bar{U}_1$ represents all the remaining terms on the left-hand side of Eq. (25). Note that the above procedure does not require the explicit evaluation of the matrix inverse $(\partial \bar{\bar{E}}^*/\partial \bar{\bar{U}})^{-1}$. Equations (28a) and (28c) represent block tridiagonal systems of equations which are solved using a routine written by Steger (27). Also, artificial dissipation in the form of an explicit fourth-order smoothing term and an implicit second-order smoothing term has been added to the algorithm as described in Ref. 6.

IV. BOUNDARY CONDITIONS

At each ξ station, the computational domain (i.e., the (η, ζ) solution surface) is bounded by the outer bow shock and the inner body surface. For symmetrical flows, with no yaw, only one-half of the computational domain needs to be considered, since the other half is known from symmetry.

The flow conditions at the shock boundary are computed using a "shock fitting" technique developed for the generalized coordinate system. The present shock fitting scheme is based on the technique of Thomas et al. (28). The present shock fitting procedure is described in Appendix C. Since it is an explicit method, it may place limitations on the maximum step size.

At the inner wall boundary, the velocity components are set equal to zero and the wall temperature is either specified for the case of an isothermal wall or it is computed using a one-sided difference approximation for a zero normal temperature gradient when the wall is adiabatic. By setting the normal pressure gradient equal to zero (which is a valid assumption very close to the wall), the density at the wall is calculated using the equation of state. All the wall boundary conditions are imposed implicitly.

At the plane of symmetry, reflection boundary conditions are imposed implicitly and the flow symmetry is maintained for zero yaw angle cases.

V. NUMERICAL SOLUTION TO THE FLOW

AROUND A SLAB DELTA WING

As a first test case and to validate the code, the generalized PNS code has been used to compute the laminar flow over a 70° sweep slab delta wing having a spherical nose and a cylindrical leading edge. Figure 1 shows the body shape. The body shape and the initial conditions were chosen to match the experiments of Bertram and Everhart (29). These experiments were conducted in the Langley 11-inch Hypersonic Tunnel at Mach numbers of 6.8 and 9.6 using air.

A. Initial Conditions

The PNS solver requires an initial data surface to start the space marching procedure. The inviscid flow region, on this initial data surface, must be supersonic and the streamwise component of the velocity must be positive. The nose portion of the slab delta wing is spherical. Hence, the flow around this spherical nose region is computed with an axisymmetric, time-dependent, Navier-Stokes code (30). The resulting solution was then recast in terms of the coordinates used in the PNS code to provide the three-dimensional starting data. The present use of an axisymmetric code to produce three-dimensional starting data was possible because the initial portion of the flow over a body with a spherical nosecap is axisymmetric about the wind axis provided that the spherical cap extends into the supersonic region of the flow. All of the cases considered for this particular problem satisfy this criterion.
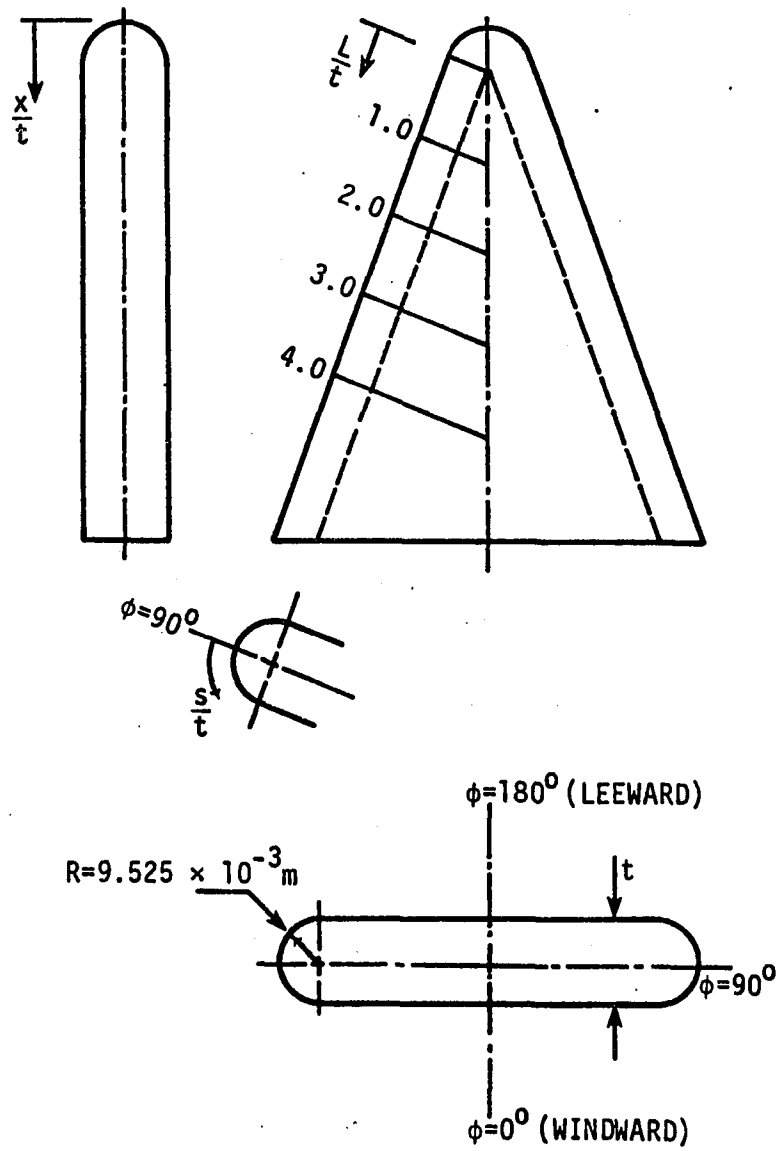
Figure 1. Slab delta wing with 70° sweep

B. Grid Generation

At each ξ station, the physical plane was chosen to be a plane normal to the leading edge. The outer boundary is chosen as the bow shock and the inner boundary coincides with the body curve. Since the flow is symmetrical, the two remaining boundaries are chosen as the symmetry planes on the windward and leeward sides of the body. The computational grid in each (η, ζ) plane is formed as follows. The ζ = constant lines are generated using straight line rays which emanate from the NJ grid points situated along the body surface. The direction of each ray from the body grid point at (x_b, y_b, z_b) is given by the unit vector $\vec{n}$ (which need not be a surface normal vector). Along each ray, NK grid points are positioned. These NK grid points are clustered near the wall in order to properly resolve the viscous layer adjacent to the wall. The length of each ray represents the shock stand-off distance (δ) which is determined at each step from the shock boundary condition. The generalized coordinates (ξ, η, ζ) are defined in such a way that at each ξ station, the (η, ζ) solution surface in the physical space is mapped into the shape of a unit square in the computational plane (see Figure 2). The grid in the computational plane has uniform spacing in each direction given by

$$\Delta\eta = \frac{1}{NK - 1} \; , \; \Delta\zeta = \frac{1}{NJ - 1} \tag{29}$$

so that $\eta = (k - 1)\Delta\eta$ and $\zeta = (j - 1)\Delta\zeta$. The physical and computational planes are related by the following equations, where $s(k)$ is the stretching function
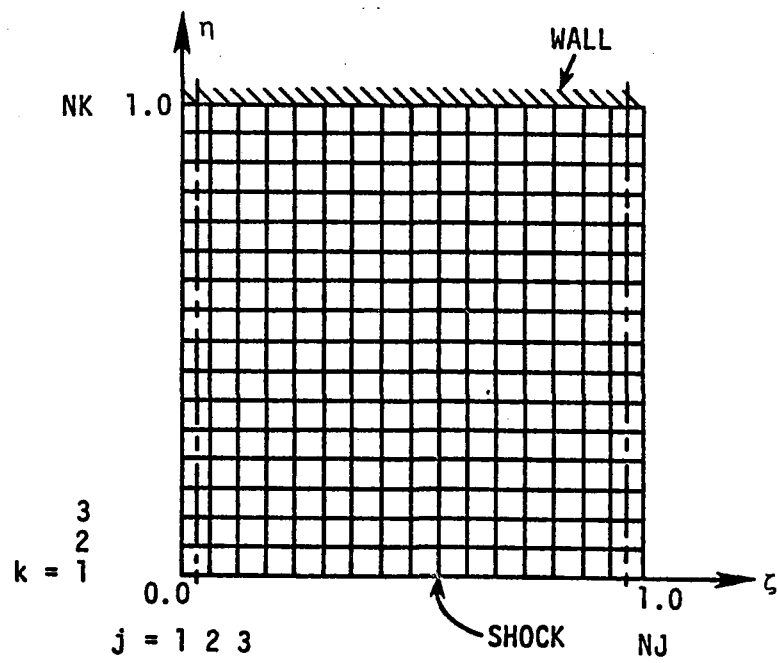
Figure 2.   Computational plane

$$s(k) = 1 - \beta\left[\left(\frac{\beta+1}{\beta-1}\right)^{\eta} - 1\right]\bigg/\left[1 + \left(\frac{\beta+1}{\beta-1}\right)^{\eta}\right] \qquad (30)$$

which clusters more grid points near the wall ($\eta = 1$) as the stretching parameter β approaches one. The metrics x_η, y_η, z_η, x_ζ, y_ζ, z_ζ which appear in Eq. (17) are computed numerically with central differences in the regularly spaced computational plane. The metrics x_ξ, y_ξ, z_ξ are evaluated with the aid of the expressions

$$x_\xi = (x_b)_\xi + \delta_\xi \, s(\vec{n} \cdot \vec{i}) + \delta \, s(\vec{n} \cdot \vec{i})_\xi$$

$$y_\xi = (y_b)_\xi + \delta_\xi \, s(\vec{n} \cdot \vec{j}) + \delta \, s(\vec{n} \cdot \vec{j})_\xi \qquad (31)$$

$$z_\xi = (z_b)_\xi + \delta_\xi \, s(\vec{n} \cdot \vec{k}) + \delta \, s(\vec{n} \cdot \vec{k})_\xi$$

where $(x_b)_\xi$, $(y_b)_\xi$, $(z_b)_\xi$, $(\vec{n} \cdot \vec{i})_\xi$, $(\vec{n} \cdot \vec{j})_\xi$, $(\vec{n} \cdot \vec{k})_\xi$ are known from the body and grid geometry and δ_ξ is determined from the shock fitting procedure.

C. Results

The experiments performed by Bertram and Everhart (29) were for the following flow conditions:

Table 1. Flow conditions

	$M_\infty = 6.8$	$M_\infty = 9.6$
$\tilde{P}_\infty$	889.2 N/m^2	130.3 N/m^2
$\tilde{T}_\infty$	60.2 K	47.5 K
Re_D	2.6 x 10^5	0.8 x 10^5
$\tilde{T}_{wall}$	317 K	317 K
γ	1.4	1.4
Pr	0.72	0.72

where $\tilde{T}_{wall}$ is the wall temperature for the heat transfer tests and Re_D is the freestream Reynolds number based on the nose diameter of 1.905 x 10^{-2}m. The angle of attack varied from -2.5° to +45° in the experimental tests.

A description of the numerical cases is given in Table 2. In all of these calculations, the (η, ζ) solution surfaces were constructed using ζ = constant rays that are normal to the body surface at each grid point. Hence, each (η, ζ) solution surface is a plane described by L/t = constant as seen in Figure 1. The body grid points were distributed on the wing surface by placing an equal number of points on the top and bottom flat surfaces of the wing while the remainder of the points were spaced equally around the leading edge. A typical grid is shown in Figure 3. This grid is for the solution surface located at L/t = 4.0 in Case 8 (see Table 2) and was drawn by a computer plotter using straight line segments between grid points.

Table 2. Numerical cases

Case	M_∞	α	Wall boundary condition	Grid (NJ x NK)	β
1	6.8	0°	Adiabatic	24 x 40	1.04
2	6.8	0°	Isothermal	24 x 40	1.04
3	6.8	10°	Adiabatic	24 x 40	1.04
4	9.6	0°	Adiabatic	18 x 40	1.04
5	9.6	0°	Isothermal	18 x 40	1.04
6	9.6	5°	Isothermal	24 x 40	1.04
7	9.6	20°	Adiabatic	25 x 40	1.04
8	9.6	41.5°	Adiabatic	25 x 40	1.04

The computed results are too numerous to show in their entirety. Instead, a representative sampling of the results is presented. The computed shock shapes for M_∞ = 9.6 at angles of attack of 0°, 20° and 41.5° are shown in Figures 4-8 along with the corresponding experimental shock shapes. Figures 4-7 show both the side and planform views of the shock at α = 0° and α = 20°. Figure 8 shows the side view of the shock computed at α = 41.5° and this is compared to the experimental shock shape obtained at α = 40°. The corresponding planform view is not given since the experimental shock shape was distorted by tunnel-wall flow separation. In all cases, the computed shock shapes are in excellent agreement with the experimental results. Both the experiment and the present numerical study indicate that the shock shape is relatively insensitive to Mach number.
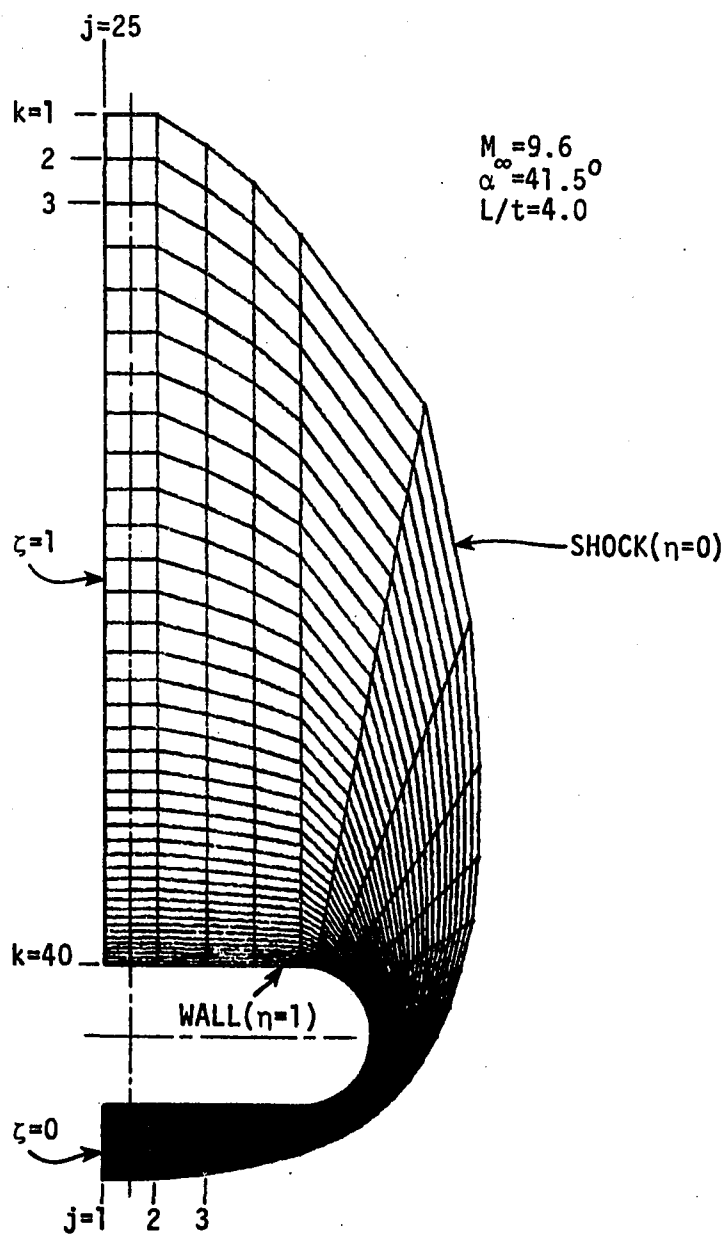
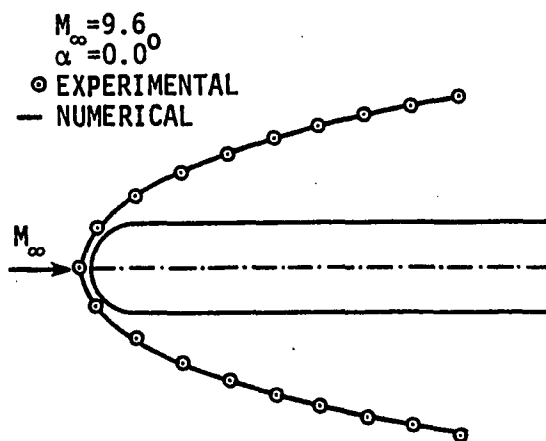Figure 3. Typical grid
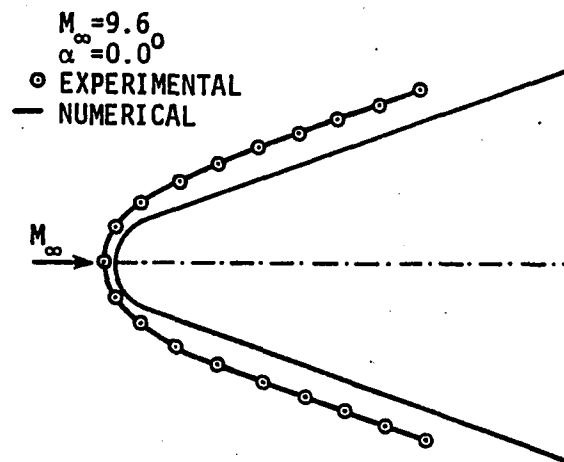
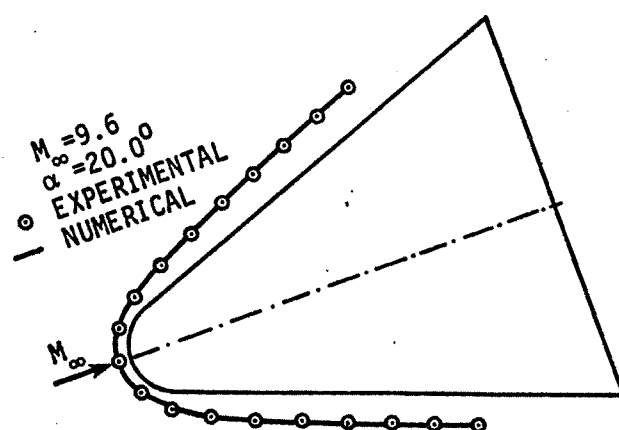Figure 4. Shock shape (Case 4)

Figure 5. Shock shape (Case 4)

$M_\infty = 9.6$
$\alpha_\infty = 20.0^\circ$
⊙ EXPERIMENTAL
— NUMERICAL

M_∞

Figure 6. Shock shape (Case 7)

$M_\infty = 9.6$
$\alpha_\infty = 20.0^\circ$
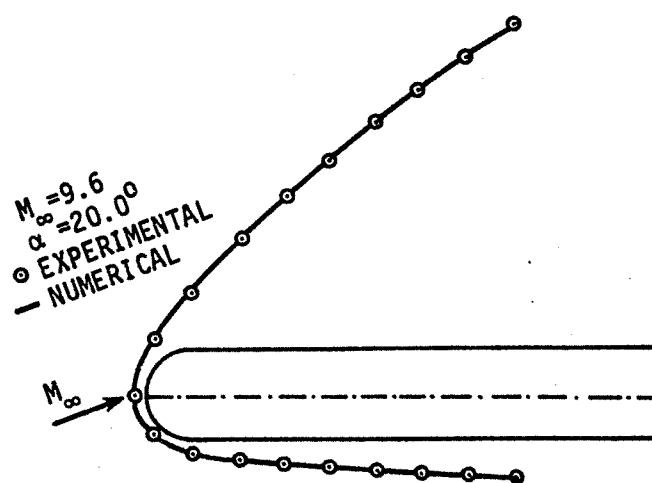⊙ EXPERIMENTAL
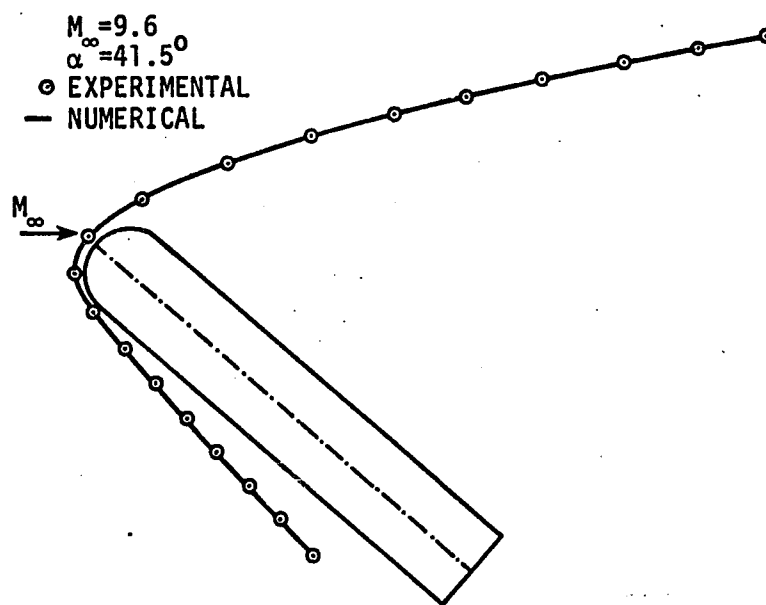— NUMERICAL

M_∞

Figure 7. Shock shape (Case 7)

Figure 8. Shock shape (Case 8)

The wall pressures for several different cases are given in Figures 9-12. These results were obtained by assuming an adiabatic wall in order to match the experimental conditions. The wall pressures are plotted as functions of the nondimensionalized distance (s/t) which is measured along the body surface from the leading edge in a L/t = constant plane. The nondimensional distance (s/t) is positive on the windward side of the wing and is negative on the leeward side. Figure 9 shows the wall pressure at L/t = 3.0 for Case 1; Figure 10 shows the wall pressure at L/t = 4.0 for Case 3; Figure 11 shows the wall pressure at L/t = 2.0 for Case 7; and Figure 12 shows the wall pressure at L/t = 4.0 for Case 8. In all the cases presented here, as well as for the cases not presented, the computed wall pressures are in good agreement with the experimental values.

Heat transfer coefficients for two cases are shown in Figures 13-15. The heat transfer coefficients are normalized using either the leading edge heat transfer coefficient (h_c) or the maximum heat transfer coefficient (h_{max}) in the given L/t plane. Figure 13 shows the distribution of the heat transfer coefficient at L/t = 2.0 for Case 2. Figures 14 and 15 show the distributions at L/t = 2.0 and 3.0 for Case 6. The computed heat transfer coefficients agree reasonably well with the experimental coefficients.

The Cartesian cross-flow velocity directions are shown in Figure 16 for Case 7 at L/t = 5.025. The primary vortex above the wing is clearly evident in this figure. Also, a small secondary vortex is just barely visible near the surface of the wing. Figure 17 shows the Cartesian cross-flow velocity directions for Case 8 at L/t = 4.0. The
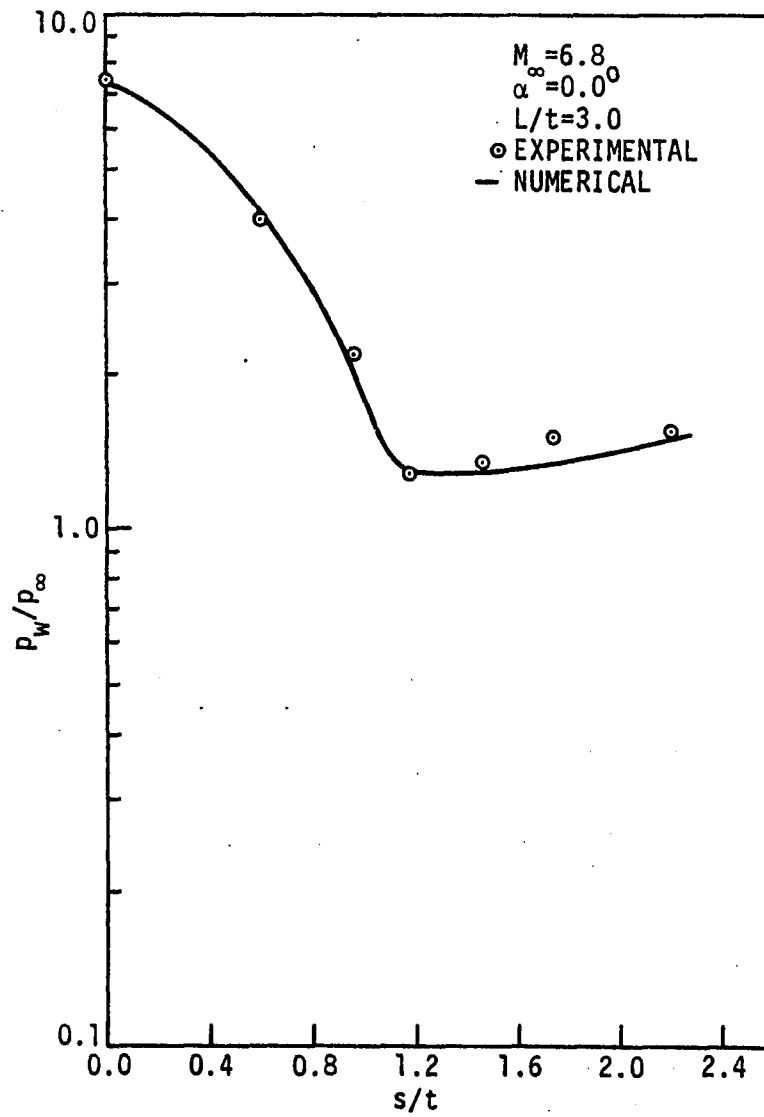
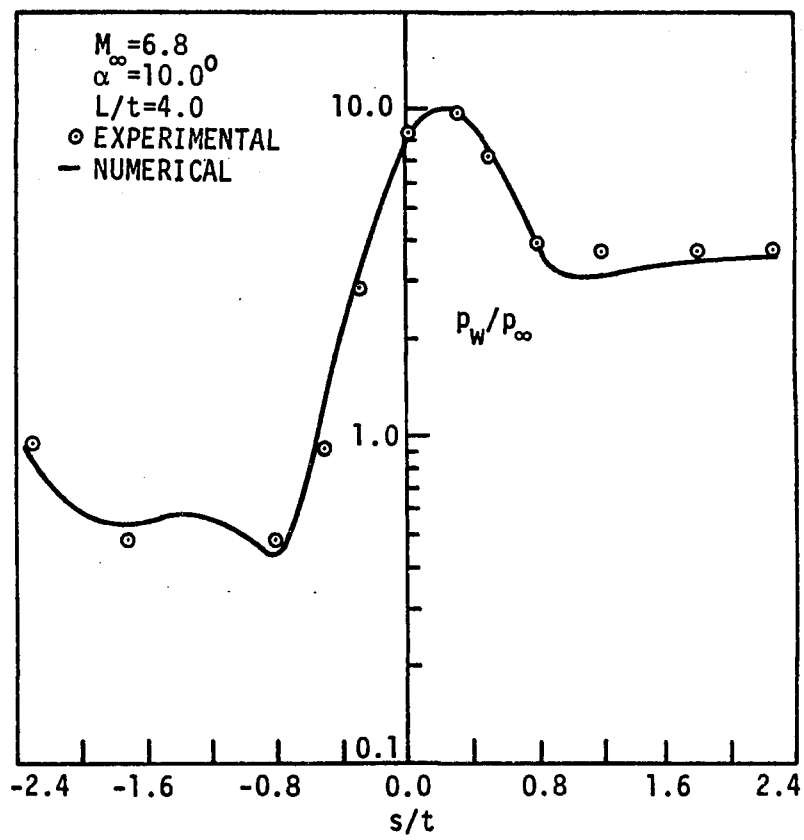Figure 9. Comparison of wall pressures (Case 1)

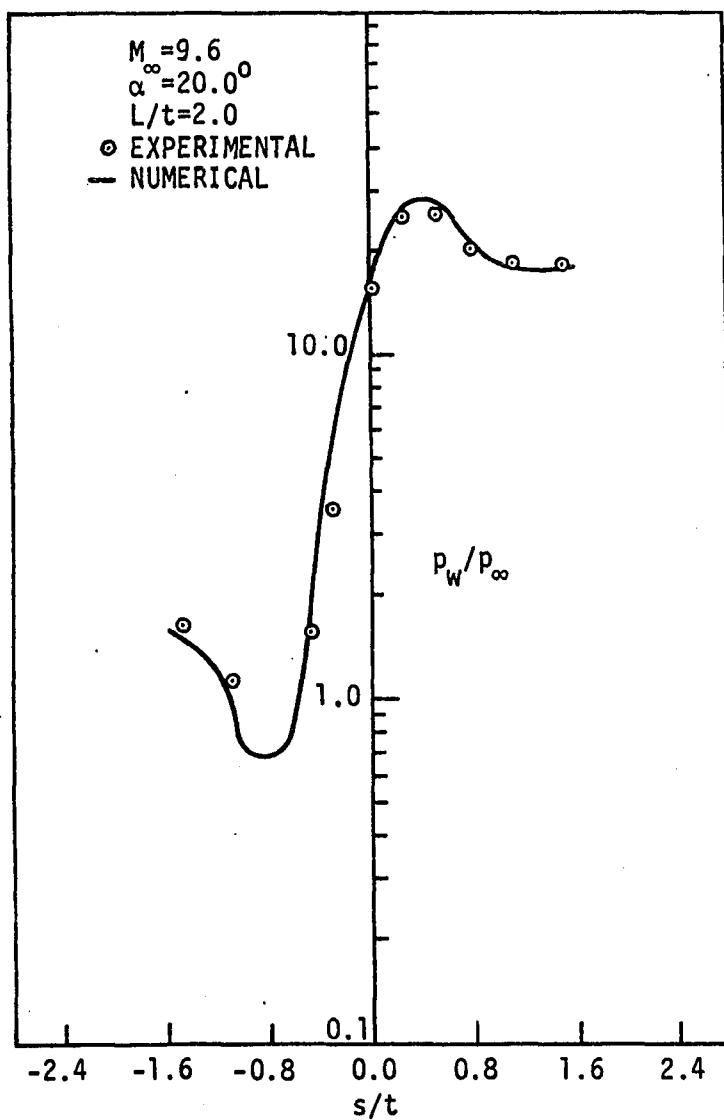Figure 10. Comparison of wall pressures (Case 3)

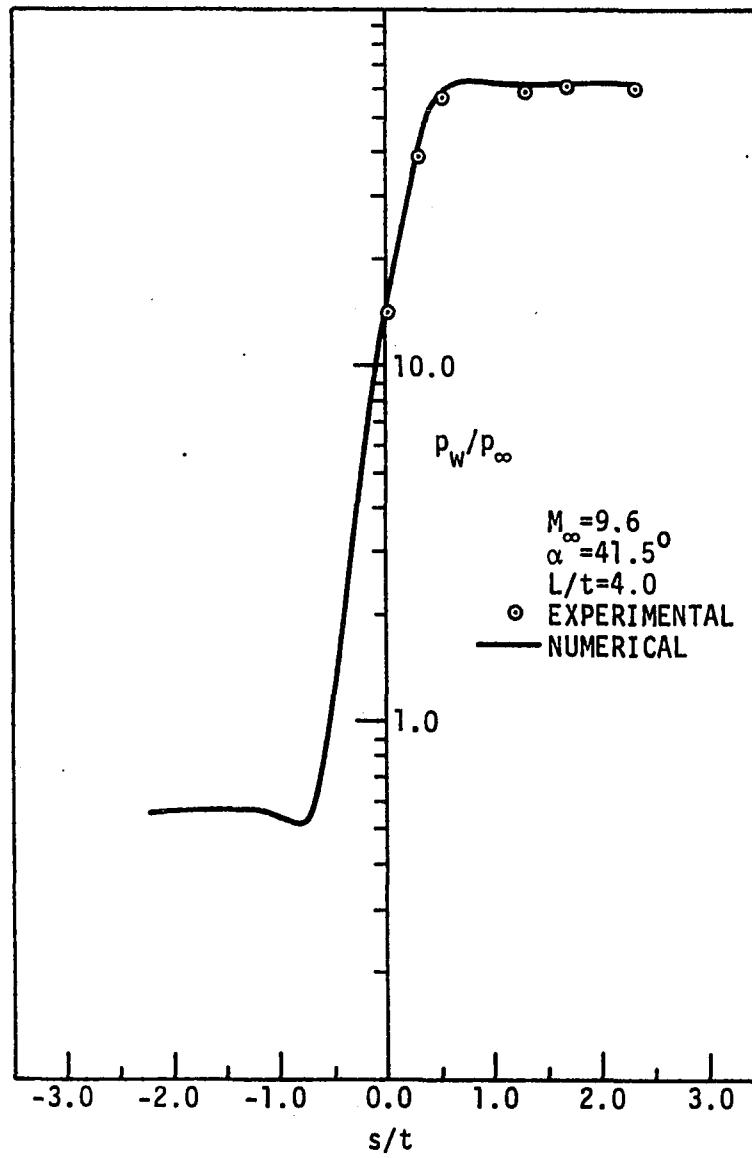Figure 11. Comparison of wall pressures (Case 7)

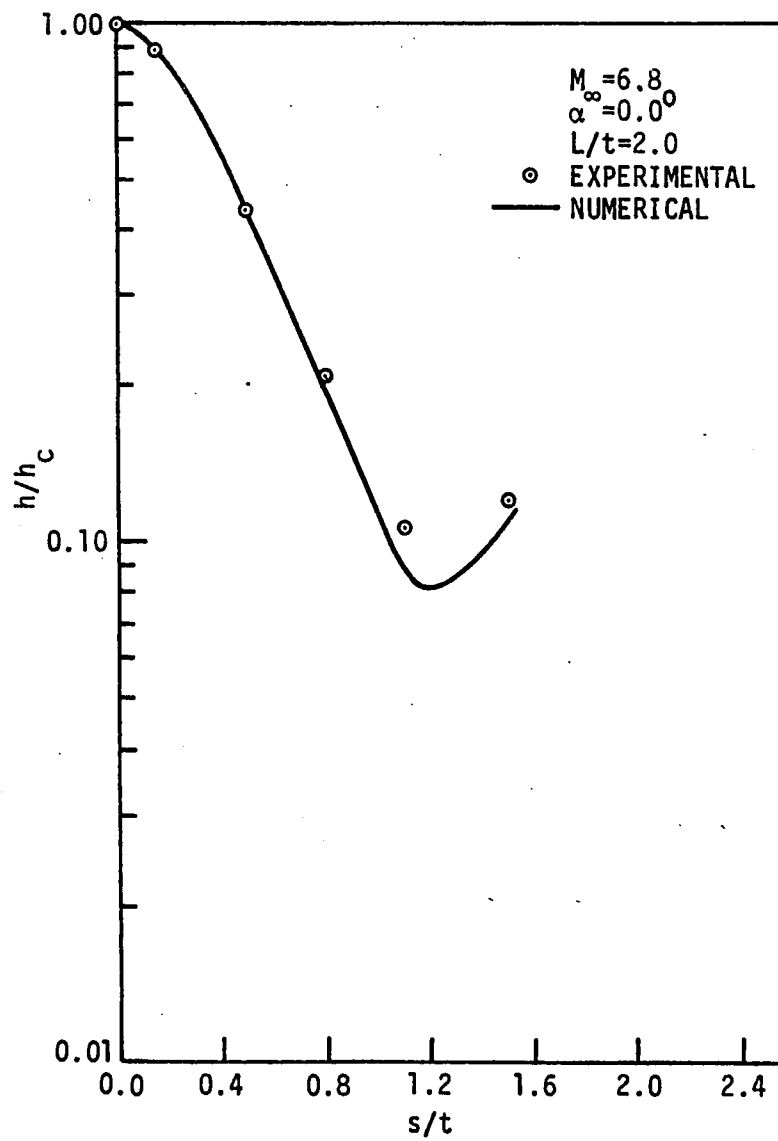Figure 12. Comparison of wall pressures (Case 8)

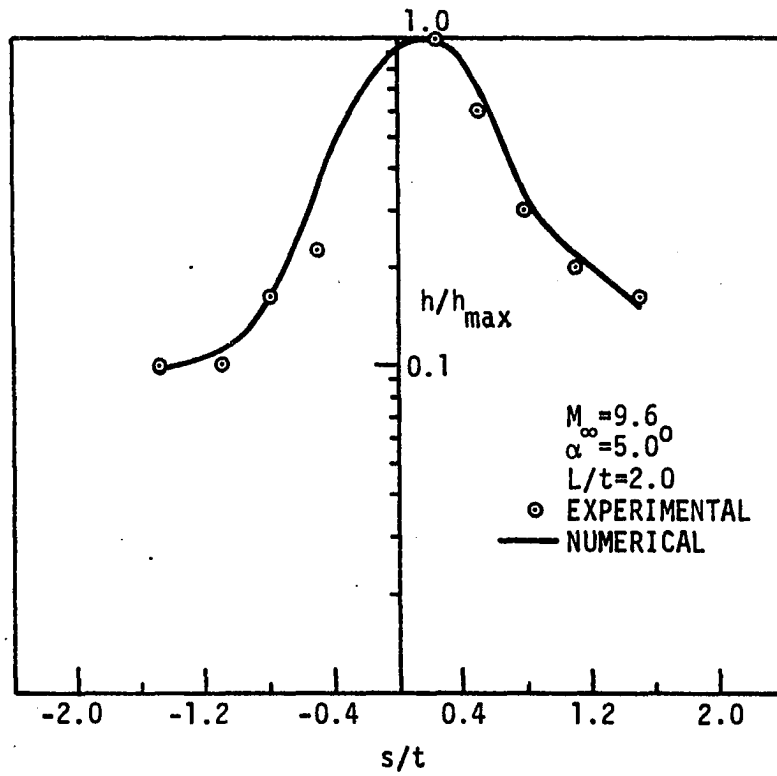Figure 13. Comparison of heat transfer coefficients (Case 2)

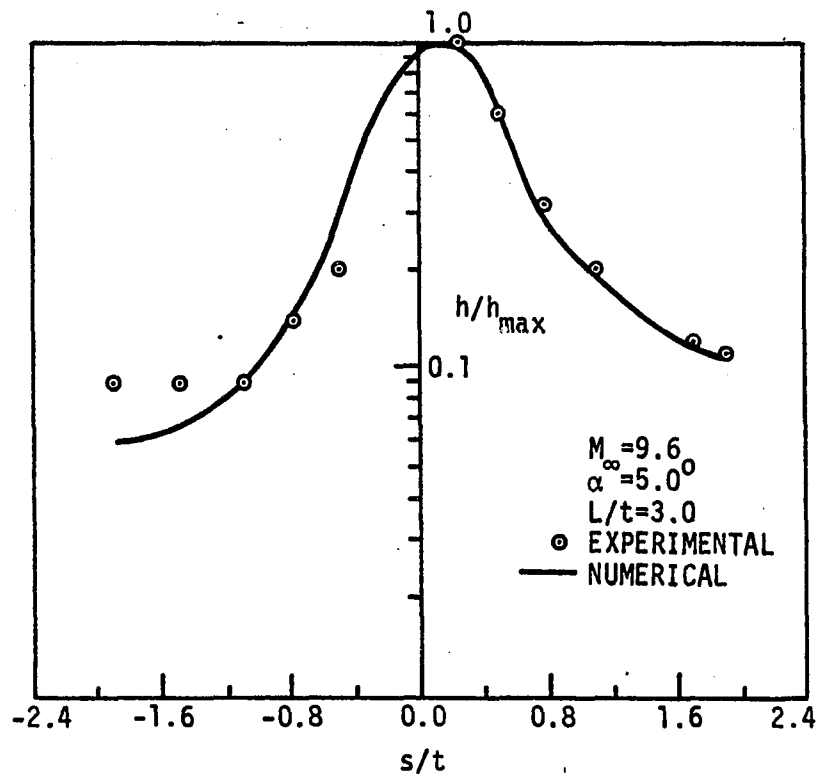Figure 14. Comparison of heat transfer coefficients (Case 6)

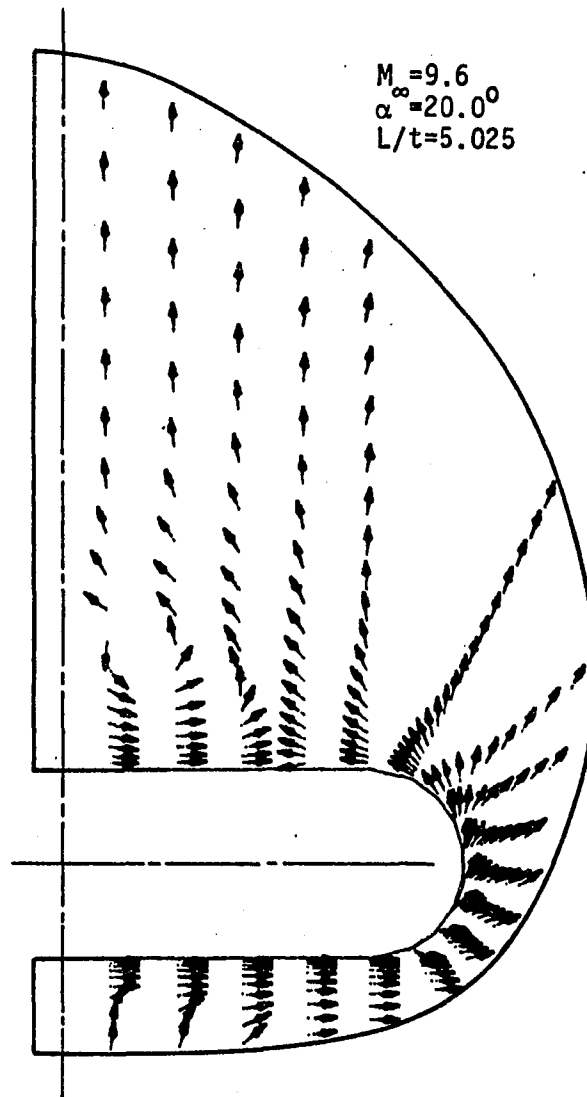Figure 15. Comparison of heat transfer coefficients (Case 6)

$M_\infty = 9.6$
$\alpha = 20.0^\circ$
$L/t = 5.025$

Figure 16. Crossflow velocity directions (Case 7)

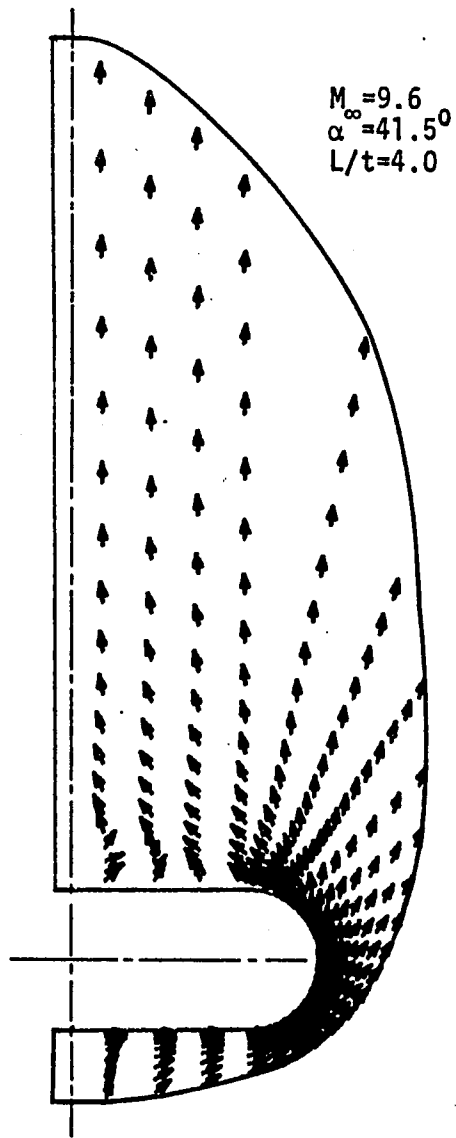$M_\infty = 9.6$
$\alpha_\infty = 41.5^0$
$L/t = 4.0$

Figure 17.   Crossflow velocity directions (Case 8)

primary vortex is not clearly defined in this case but it appears to be located near the leeward side symmetry plane.

The variations of pressure, temperature and density normal to the body surface are given in Figures 18-20 for Case 8 at L/t = 4.0. Figure 18 shows the normal variations in the windward side symmetry plane; Figure 19 shows the normal variations in the leeward side symmetry plane; Figure 20 shows the normal variations at the leading edge. No experimental data were available to compare these normal distributions.

During the computations, both the "Vigneron" technique and the "sublayer approximation" technique were used for the streamwise pressure gradient term. The difference in the results obtained using the two techniques was extremely small at the lower angles of attack. At the higher angles of attack, the calculations which employed the "sublayer approximation" technique were unstable. (It should be remembered, however, that in the present "sublayer approximation" technique, the complete streamwise pressure gradient term is retained in the energy equation in the sublayer region.) The calculations which employed the "Vigneron" technique were stable if a safety factor was applied to ω to reduce it below the value computed by Eq. (21).

The results of this study were obtained on a CDC 7600 computer. The generalized PNS code required 1.06×10^{-3} seconds of computer time per step per grid point. A typical solution, such as Case 8 (25 x 40 mesh), was obtained with 511 steps and 9 minutes of computer time.
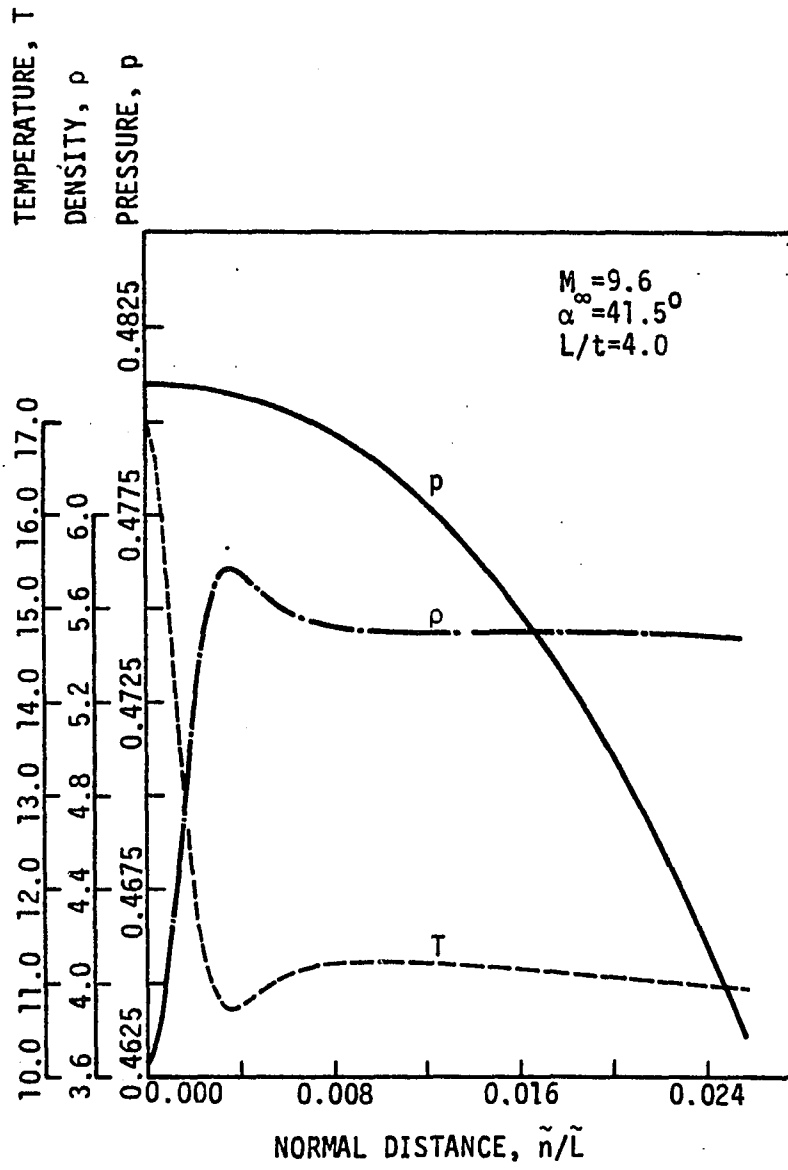
Figure 18. Variation of flow properties in normal direction at $\phi = 0^\circ$ (Case 8)
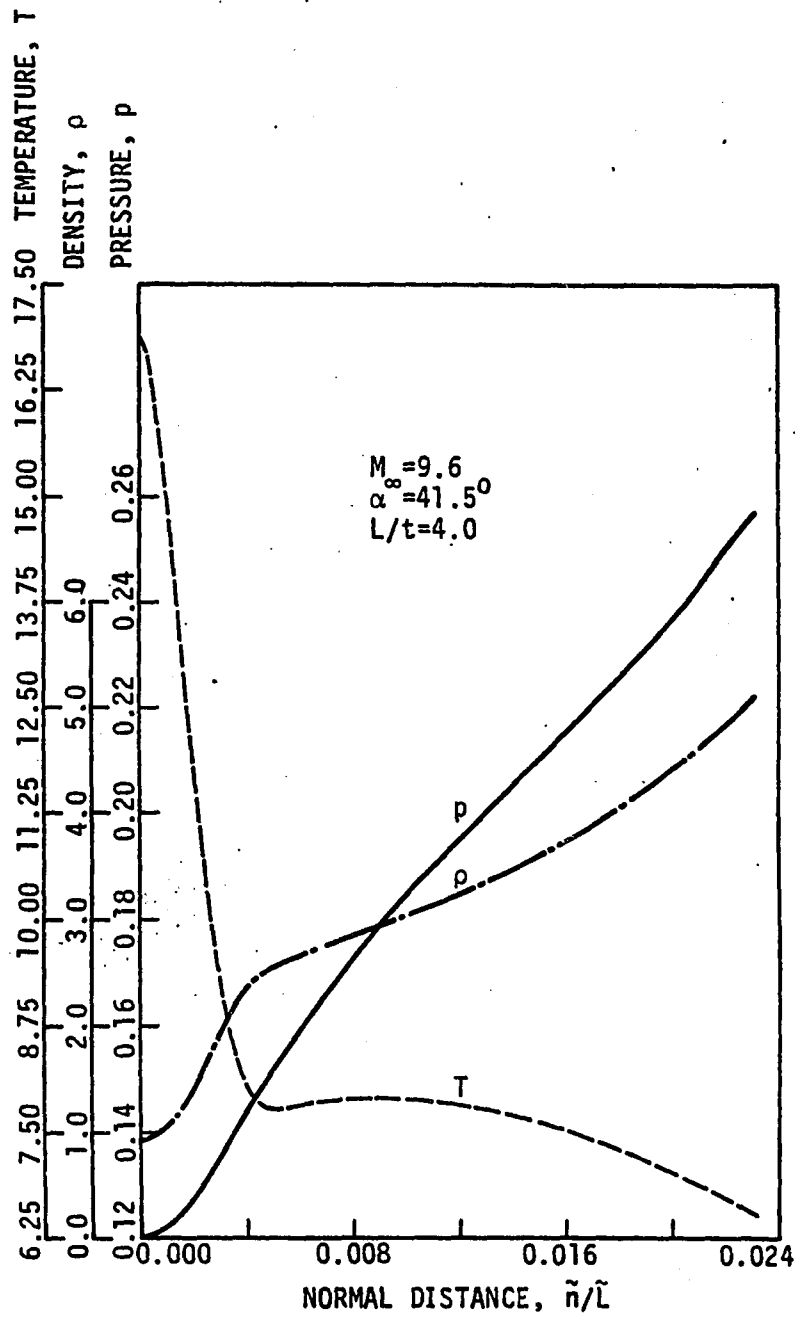
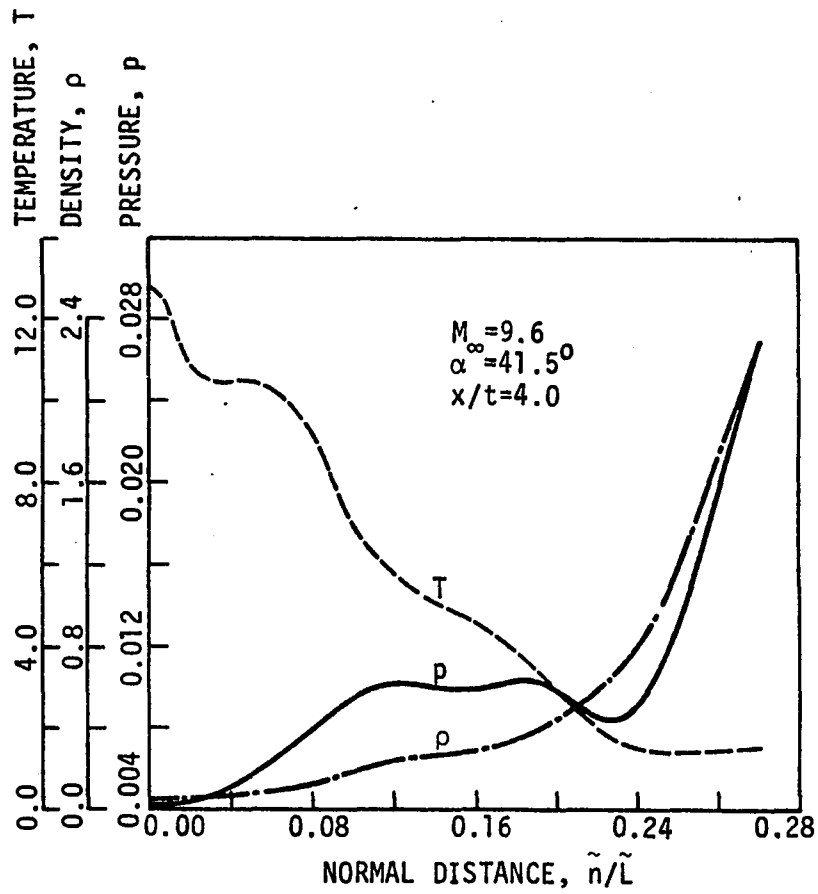Figure 19. Variation of flow properties in normal direction at $\phi = 180^\circ$ (Case 8)

TEMPERATURE, T
DENSITY, ρ
PRESSURE, p

$M_\infty = 9.6$
$\alpha = 41.5°$
$x/t = 4.0$

T

p

ρ

NORMAL DISTANCE, $\tilde{n}/\tilde{L}$

Figure 20. Variation of flow properties in normal direction at $\phi = 90°$ (Case 8)

VI. NUMERICAL SOLUTION TO THE FLOW

AROUND THE SPACE SHUTTLE ORBITER FOREBODY

The excellent numerical solutions to the slab delta wing case
proved that the generalized PNS solver can be used to accurately pre-
dict the supersonic viscous flow around smooth shaped bodies. The Space
Shuttle Orbiter flow field, however, presents special problems due to
its geometric complexity. In this case, the full capabilities of the
generalized PNS solver are used advantageously. The use of a generalized
coordinate transformation allows the construction of skewed solution
surfaces. Also, the solution domain for the blunt nose region when using
the three-dimensional time-dependent code is limited by the sonic surface
and not by the PNS solver. Hence, the amount of computer time re-
quired to solve the unsteady blunt nose problem is reduced consider-
ably.

A. Space Shuttle Orbiter Geometry

The Space Shuttle Orbiter geometry is a complex three-dimensional
body shape. The presence of wing, wing body juncture and other details
have to be described accurately. The coordinate locations of the grid
points on the Shuttle surfaces are obtained with the geometry package
developed and used by Rakich et al. (9). This geometry package repro-
duces the Shuttle Orbiter geometry exactly at eleven different axial
locations, and intermediate to these locations, interpolation poly-
nomials are used to produce the actual Space Shuttle Orbiter geometry
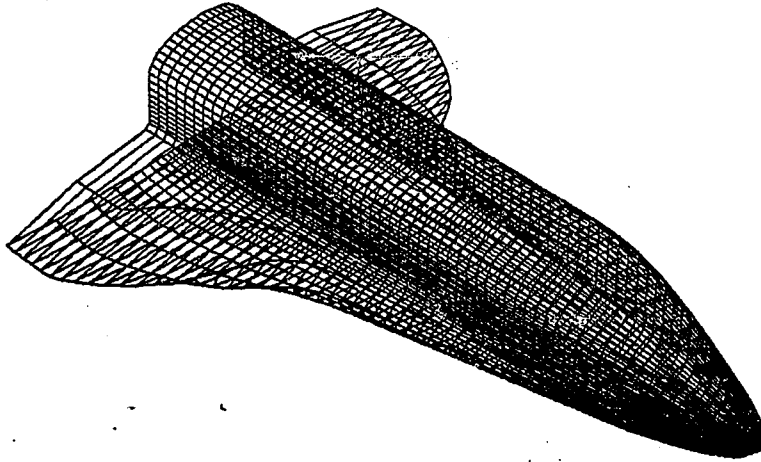very closely. Figure 21 shows a three-dimensional and cross-sectional
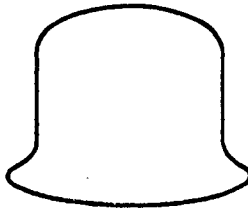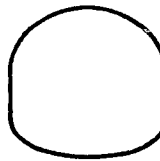
SHUTTLE GEOMETRY

X = 900IN.   X = 500IN.   X = 200IN.

Figure 21. Space Shuttle Orbiter geometry

view of the Space Shuttle Orbiter obtained with the above geometry

package. Complete details of the geometry package used in this study

are given in Refs. 31 and 32. Note that the present Space Shuttle

Orbiter geometry does not include the canopy or the vertical tail

region. The presence of the canopy forces the flow to separate in the

streamwise direction. Since the PNS solver cannot handle streamwise

flow separation, the canopy is removed from the Shuttle geometry, in

this study.

B. Grid Generation

To obtain the correct numerical solution, a proper grid needs to

be used. Numerous grid generation methods are available in the

literature. The PNS method requires the grid to be generated at every

ξ station and this demands the use of a fast grid generation scheme.

A simple and efficient algebraic grid generation scheme is used

in the present study which allows the grid points on the body and

shock curves to be clustered in regions of high curvature. This is

accomplished in the following manner. The inner body boundary curve or

the outer shock boundary curve is parameterized by a nondimensional arc

length parameter, δ, in the physical plane. In the computational plane,

the corresponding parameter that represents the inner or outer boundary

curve is ζ. The relationship between ζ and δ, which is referred to as

the "stretch function," maps the equispaced grid points in the computa-

tional region into the nonequispaced grid points on the inner or outer

boundary curve in the physical plane. Initially, it seemed appropriate

to cluster the grid points in regions of high curvature. This approach

gives the following stretch function,

$$\left(\frac{\partial \zeta}{\partial \delta}\right)_i = 1 + \sum_{j=1}^{N} A_j(K) \left\{ 1. + \tanh \left[\frac{(\delta_i - \delta_i)}{B_j(K)} \right] \right\} \tag{32}$$

where

$$A_j(K) = K/K_{max}$$

$$B_j(K) = (1. + K/K_{max})$$

K = local curvature corresponding to the jth point

N = total number of points that describes the curve

i, j = integer values corresponding to grid points

Unfortunately, the above stretch function does not allow the user to

choose the desired clustering and yields unrealistic grids. However,

the general stretch function given by Eq. (32) can be modified to the

following form which permits the user to tailor the clustering to the

requirements of each flow field.

$$\left(\frac{\partial \zeta}{\partial \delta}\right)_j = A_1 \left\{ 1. + \tanh \left[\frac{(\delta_j - \delta_1)}{B_1} \right] \right\}$$

$$+ A_2 \left\{ 1. + \tanh \left[\frac{(\delta_j - \delta_2)}{B_2} \right] \right\} \tag{33}$$

where A_1, A_2, B_1, and B_2 are user specified constants and δ_1 and δ_2 are

the arc length values corresponding to locations where clustering is

required. Depending on the sign and magnitude of A_1 and A_2, the above

stretch function either clusters the grid points closer to one another

or stretches it away at the corresponding δ_1 and δ_2 arc length locations.

The relationship between δ and ζ is determined by numerically integrating

Eq. (33). This relationship coupled with the fact that the grid points are equispaced in the computational plane determines the exact location of the grid points in the physical plane.

Figure 22 shows the clustered grid points for the Orbiter geometry and the corresponding stretch function that was used to cluster the grid points. The grid generation is accomplished using the above stretch function approach in three steps.

1. The grid points on the inner body boundary curve are located using the algebraic stretch function approach.

2. The shock boundary curve is completely determined from the known solution at the previous station. Hence, the shock boundary grid points are determined from the user prescribed solution surface orientation. The grid points on the shock boundary can be reclustered, if required, using the stretch function approach.

3. Interior grid points are located along the straight line rays that connect the appropriate body and shock boundary points. An algebraic stretch function [Eq. (30)] clusters the grid points along each of the rays near the body surface in order to resolve the viscous region properly.

The above three steps determine all the grid points in the physical plane. The interior grid points in the physical plane are related to the body grid points by Eq. (31). The grid point location in the computational plane is determined by the following relationships

$$\eta = (k - 1)\Delta\eta, \qquad \Delta\eta = \frac{1}{NK - 1}$$

$$\tag{34}$$

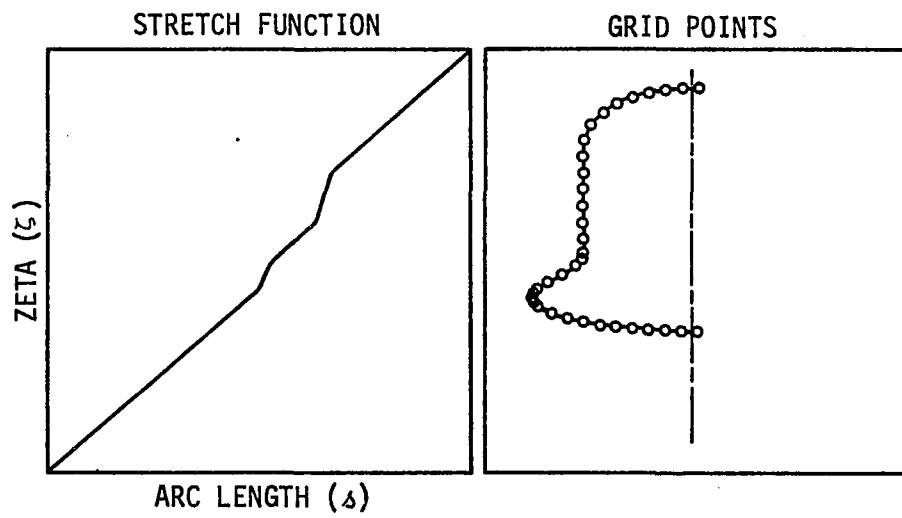$$\zeta = (j - 1)\Delta\zeta, \qquad \Delta\zeta = \frac{1}{NJ - 1}$$

Figure 22. Stretch function and the grid points

where NK is the number of grid points between the body and shock, and k

is an integer parameter that varies from k = 1 at the shock to k = NK

at the body. NJ is the number of grid points around the body and j is

an integer parameter that varies from j = 1 on the windside to j = NJ

on the leeside.

Once the location of all the grid points are known, both in the physi-

cal and the computational domains, the geometric metric quantities and

the Jacobian of the transformation are computed by finite difference

approximations (8). The Jacobian and the metric quantities are first-

order accurate in ξ and second-order accurate in ζ and η. This is

consistent with the difference scheme used in the present study.

C. Solution Surface Marching

In the slab delta wing case, the solution surfaces were planes

normal to the leading edge of the wing. In the present computation,

the initial solution surface obtained from the blunt body code is a

skewed surface. Since the present formulation does not restrict the

solution surface in any manner, these surfaces can be generated based

on local flow conditions best-suited for PNS marching. The proper choice

of the orientation of the solution surfaces is determined by the ap-

propriate direction of marching. In effect, the user can control the

direction of marching by specifying the orientation of the solution

surface at each ξ station. In the present computation, the solution

surfaces are advanced from the prescribed initial solution surface to a

location surface normal to x-axis at a specified x location. This is

accomplished by independently changing the orientation of the vectors that describe the body grid points and the vectors that connect the body and shock grid points. The marching step size becomes different for each grid point in the physical plane. Once the solution surface has become an axis normal plane, it is maintained axis normal in the present study. Figure 23 shows the solution surface at different ξ stations and explains how the solution surfaces are marched downstream.

D. Blunt Nose Solution and Initial Conditions

The PNS code requires a starting solution on an initial data surface where the inviscid flow is supersonic. The presence of an embedded subsonic region in the blunt nose region requires the use of an axisymmetric or three-dimensional time-dependent Navier-Stokes code for finding the blunt nose solution. The three-dimensional blunt body code originally developed by Kutler et al. (33) and later modified by Rizk et al. (34) is used here to obtain the blunt nose starting solution for the PNS code.

The blunt body code requires an initial solution or an approximate shock shape. In the past, a converged solution at a lower angle of attack was used as the starting solution for a higher angle of attack case. Due to the slow convergence and the enormous computer time required by the blunt body code, it was necessary to solve the 30 degree angle of attack case without obtaining a converged solution at a lower angle of attack. From the experimentally available shock shapes on the wind and lee sides, an approximate shock shape was constructed
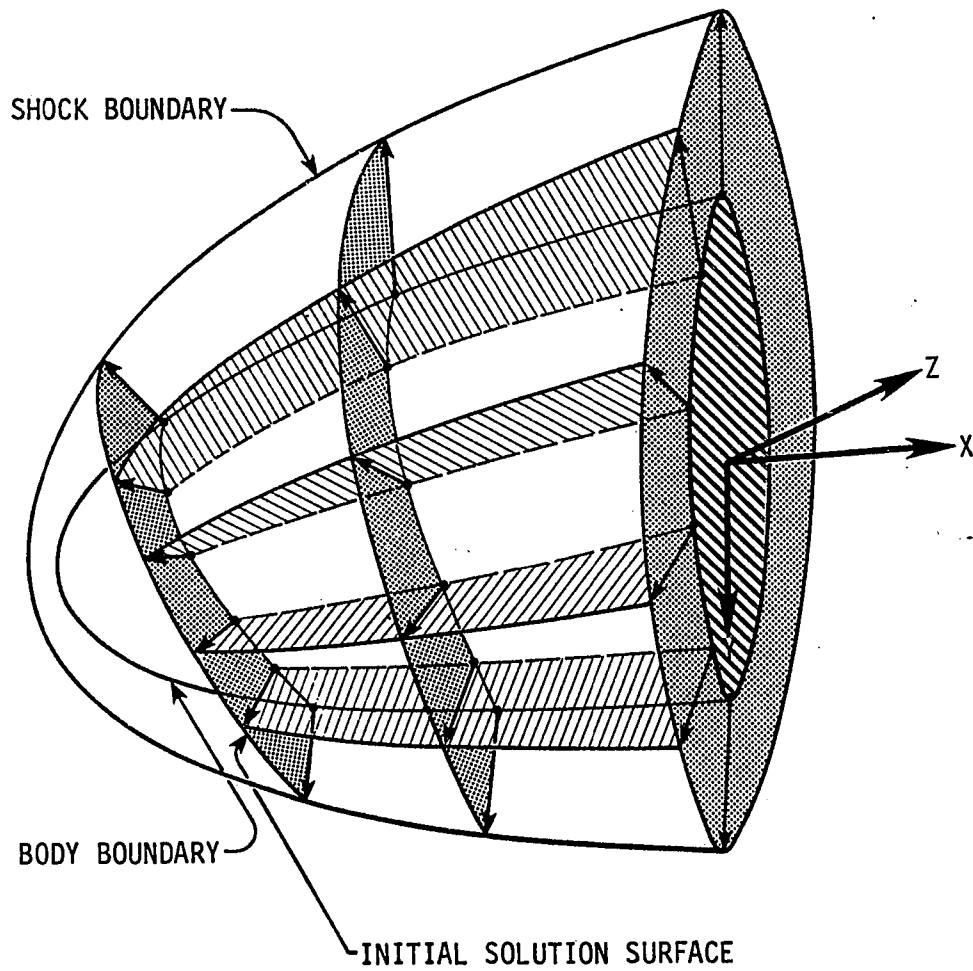
Figure 23. Solution surface marching

for the 30 degree angle of attack case. It was found that the viscous solution converged in the wind-axis coordinate system, but the solution diverged in the body-axis coordinate system. The solution convergence in the wind-axis system is due to the peculiarity in the boundary condition procedure of this blunt body code. When the physical domain is mapped into a computational cube, a singular line exists in the physical domain where a branch cut has been made. This singular line transforms into a face of the computational cube. On this singular line, the boundary conditions are applied by averaging the flow quantities about this line. If the singular line is not close to the stagnation line (the line from the stagnation point along the wind axis), then the particular boundary condition becomes incorrect and the solution diverges. If the starting solution is close to the actual solution or if a wind-axis coordinate system is used (in which case the singular line coincides closely with the stagnation line), the boundary condition procedure is correct and the solution converges. A similar approach has been taken by Rizzi and Bailey (35).

The blunt body code generally fails if the solution domain includes a large part of the lee side supersonic flow region. Also, the convergence tends to be slower if the solution domain is large. Hence, the solution domain was chosen with a small supersonic outflow boundary region on both the wind and lee sides. Since the subsonic region was highly skewed, the initial data surface was also skewed. Because of the generalized transformation used in the PNS code, the orientation of the initial data surface did not present any problems. The initial solution and the corresponding initial data plane were transformed into a

body-axis coordinate system prior to their use in the PNS solver.

Only for the 0 degree angle of attack case was the axisymmetric code of Ref. 30 used to calculate the blunt nose region. Because of the axisymmetric shape of the blunt nose body region, the required starting solution for the generalized PNS code was readily obtained in this case.

E. Results

The generalized PNS code has been used to compute the laminar flow around the forward half of the Space Shuttle Orbiter. Two different flow conditions were chosen and the results are compared with available experimental data.

The flow conditions corresponding to the first case are:

$M_\infty = 4.6$

$\alpha = 0^\circ$

$Re_L = 0.129 \times 10^7$

$T_\infty = 67.32^\circ K$

$p_\infty = 0.4556 \times 10^3 \ N/m^2$

Adiabatic wall boundary

With the above initial conditions, the solution for the blunt nose region was obtained with an axisymmetric time-dependent code (30). The Space Shuttle Orbiter nose region consists of a spherical nose segment that subtends 45 degrees at the sphere center, followed by a small conical segment which extends up to 10 inches from the nose. The axisymmetric computations were performed for a sphere-cone body with

26 grid points along the body and 31 grid points normal to the body.

The PNS computations were started with the initial solution at the end of the conical region. The PNS solution was marched downstream and the solution surfaces were rotated slowly from the initial solution surface to an axis-normal plane at $x/L = 0.125$. The step sizes and the rotation rate that would result in stable space marching were determined by trial-and-error. If the step size was too large or if the solution surfaces were rotated too fast, the solution near the shock boundary exhibited unstable behavior due to the explicit shock boundary condition procedure. If the step sizes were too small, the pressure field near the body exhibited large oscillations. This is attributed to the fact that the convergence and truncation error in the initial solution was unacceptable to the PNS solver. Marching with smaller step sizes was possible, once the solution was marched away from the initial solution surface. More points were added to the computation slowly. At an axial location of $x/L = 0.2$, the grid contained 45 grid points around the body and 41 grid points normal to the body. The space marching was continued to an axial location of $x/L = 0.48$.

Figure 24 shows the surface pressure coefficient comparison between the computed results and the experimental data (36) in the $\phi = 0^\circ$ plane. In Figure 25, the lee side ($\phi = 180^\circ$), surface pressure coefficients are compared. The agreement with the experiment is very good on both the wind and lee sides. Figures 26 and 27 show the crossflow velocity vector directions at two different axial locations, and the development of the complex flow field around the Shuttle geometry is clearly
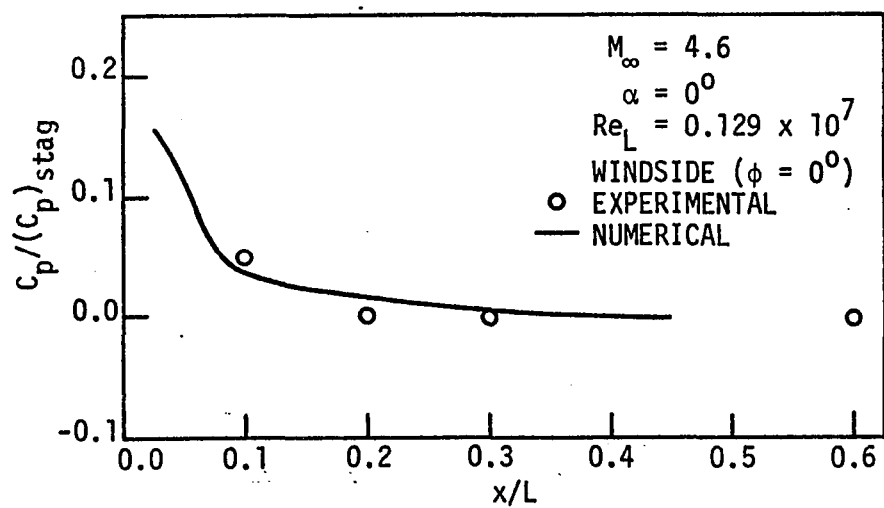
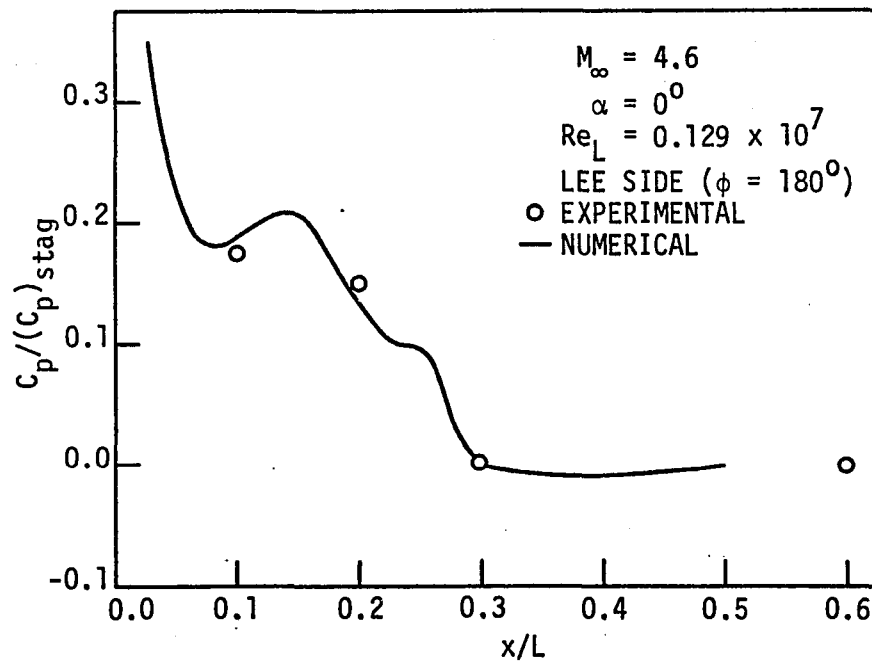Figure 24. Comparison of wind side ($\phi = 0^o$) wall pressure

Figure 25. Comparison of lee side (ϕ = 180°) wall pressure

$$M_\infty = 4.6$$
$$\alpha = 0^0$$
$$x/L = 0.2351$$
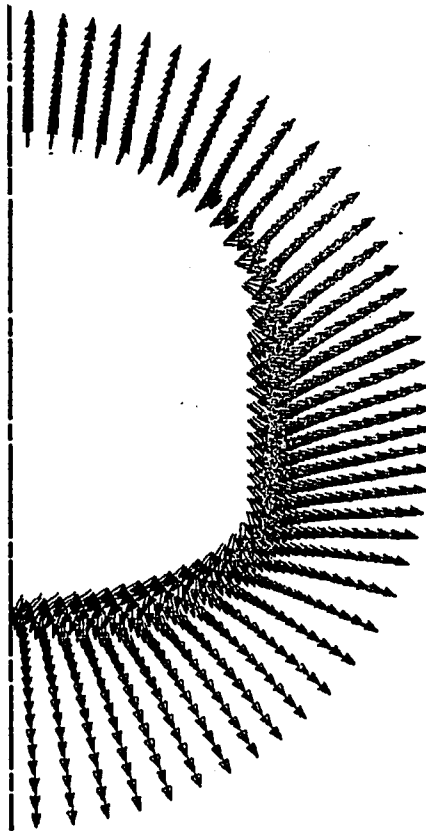
Figure 26. Crossflow velocity vector directions at x/L = 0.2351

$$M_\infty = 4.6$$
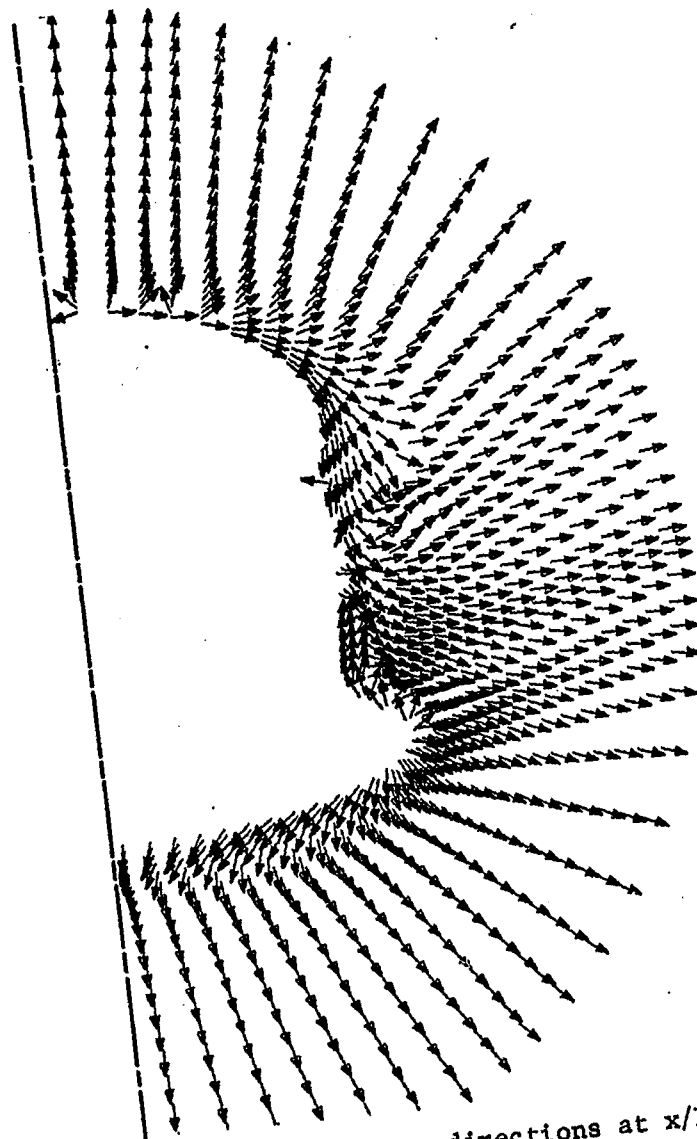$$\alpha = 0^0$$
$$x/L = 0.36$$

Figure 27. Crossflow velocity vector directions at $x/L = 0.36$

visible. At 0 degrees angle of attack, the windward side ($\phi = 0^\circ$

plane) is at a lower pressure than the $\phi = 180^\circ$ side and the stream-

lines from the lee side curve towards the wind side. As the wing starts

developing, a vortex develops near the wing body junction and this

changes the local flow pattern.

The flow conditions for the second case are:

$M_\infty = 7.9$

$\alpha = 30^\circ$

$Re_L = 0.215 \times 10^7$

$T_\infty = 52.33^\circ K$

$p_\infty = 72.95 \ N/m^2$

$T_w = 294.6^\circ K$

The time-dependent blunt body code was used to calculate the blunt nose

solution in the wind-axis coordinate system. A 31 x 31 x 21 grid was

used in the blunt body calculation. Figure 28 shows the sonic line on

the wind and lee sides. The initial solution surface for the PNS solver

was chosen as far away from the subsonic region as possible. The initial

solution surface and the solution vectors were rotated from the wind-

axis system to the body-axis system and the PNS solver was marched

downstream. The solution surfaces were rotated slowly from the initial

orientation to an x-axis normal plane at x/L = 0.20. Solutions up to

x/L = 0.48 were obtained with the PNS code.

Figure 29 compares the computed shock shape for the above flow

conditions with the experimental (37) shock shape at $M_\infty = 7.4$. The

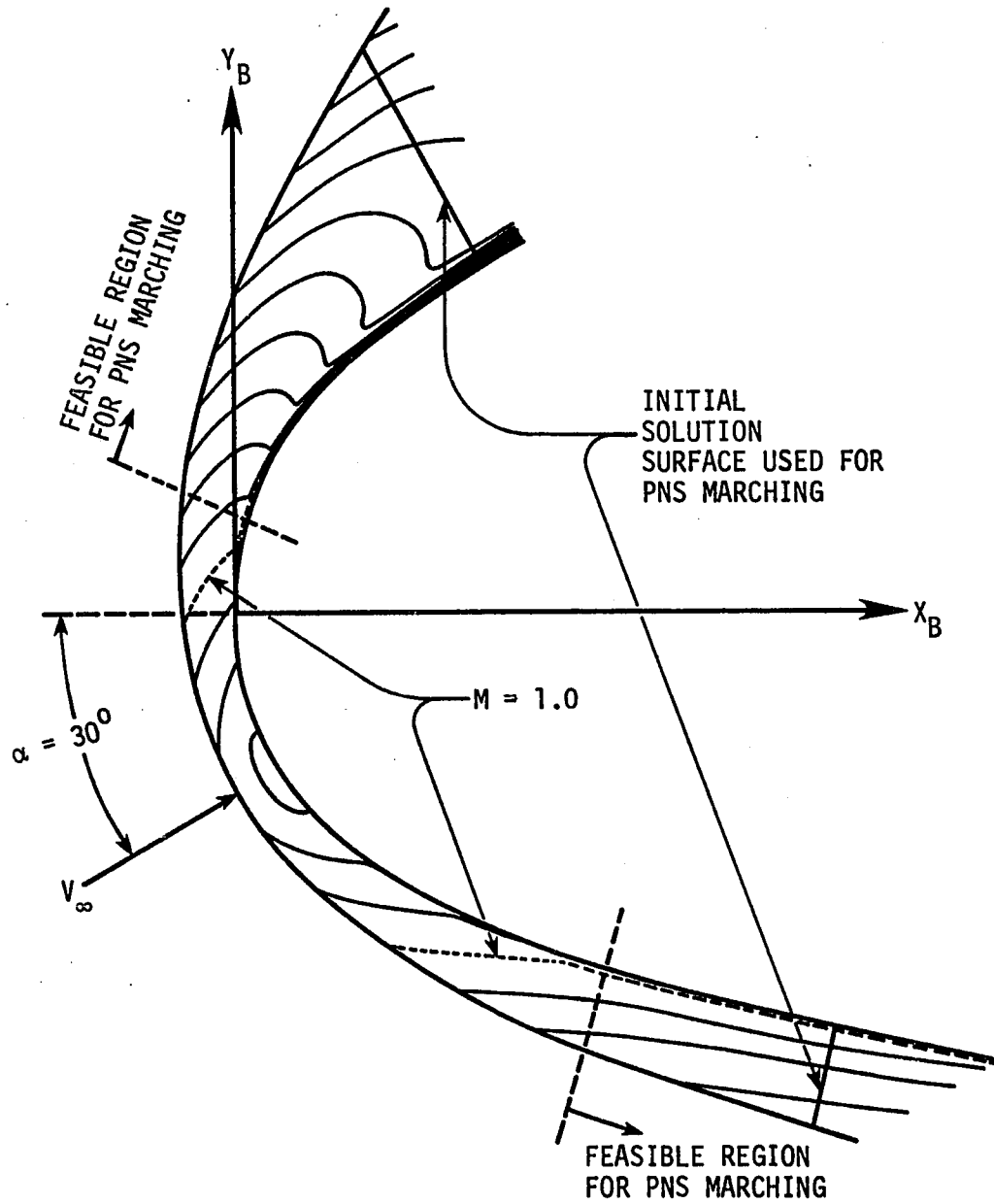Mach number difference between the experiment and the computations has

Figure 28. Mach contour plot in the blunt nose region

$M_\infty = 7.9$
$\alpha = 30^0$
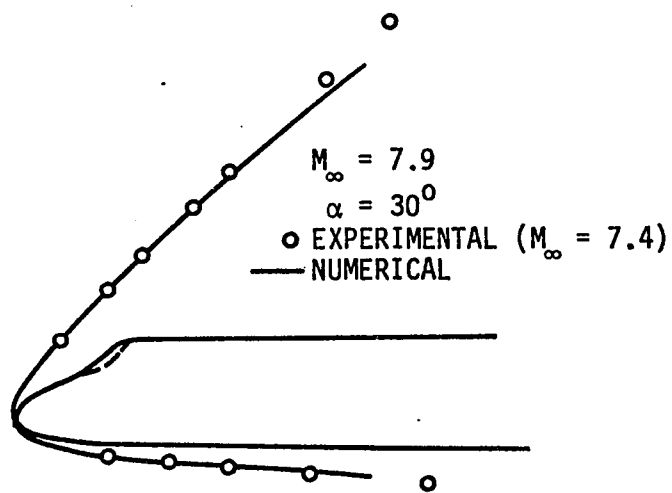o EXPERIMENTAL $(M_\infty = 7.4)$
—— NUMERICAL

Figure 29. Shock shape comparison

very little effect on the shock shape or the surface pressure coefficient profiles. Due to the presence of the canopy, a canopy shock developed in the experiment and this changed the outer shock shape on the lee side. As a result, the computational shock shape on the lee side is a little different from the experimental shock shape downstream of the canopy region.

Figure 30 shows the heat transfer coefficient comparison between the computations and the experiment (38) on the wind side. The heat transfer coefficients compare reasonably well. The heat transfer coefficient at the initial solution surface is higher than the experimental value and this is believed to be the effect of the coarse grid used in the blunt body flow field calculations. The effects of the coarse grid continue to result in higher heat transfer coefficients until x/L is approximately 0.25, where the grid is fine enough to predict good heat transfer rates. Also shown in Figure 30 are the heat transfer results with entropy swallowing predicted by Ref. 39. The agreement with the present computations is good. Figure 31 compares the computed heat transfer coefficient on the lee side with the experimental results, and the comparison is very good except near the canopy region. This was expected since the Shuttle body geometry used in the present study did not contain the canopy. Figure 32 shows the computed heat transfer coefficient vs ϕ, the circumferential angle at x/L = 0.2049. The comparison between the computed and the experimental results is fair.

Figure 33 compares the computed pressure coefficients for the above flow conditions with the experimental data at M_∞ = 7.4, both on the lee side and on the wind side planes of symmetry. Also shown in Figure 33
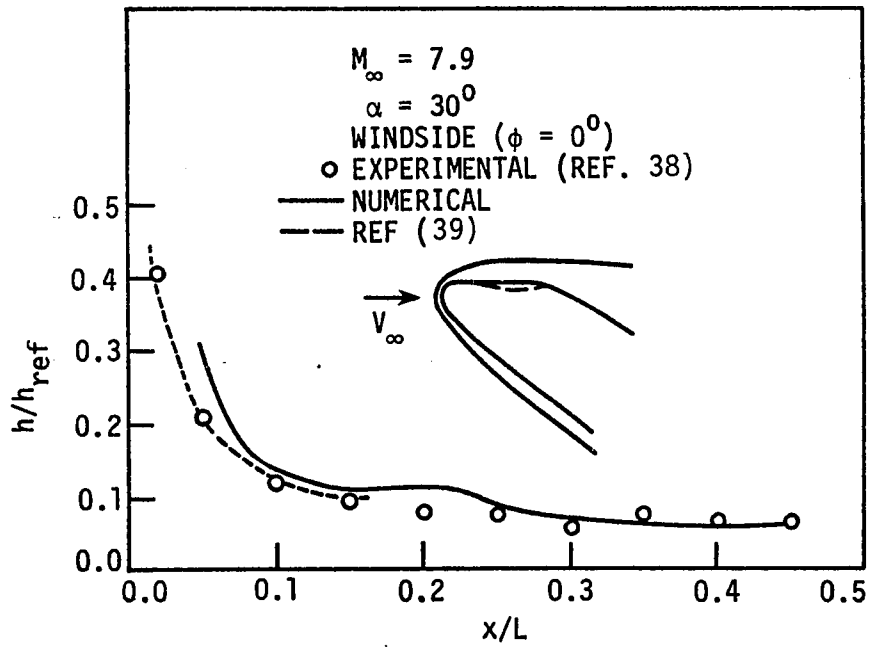
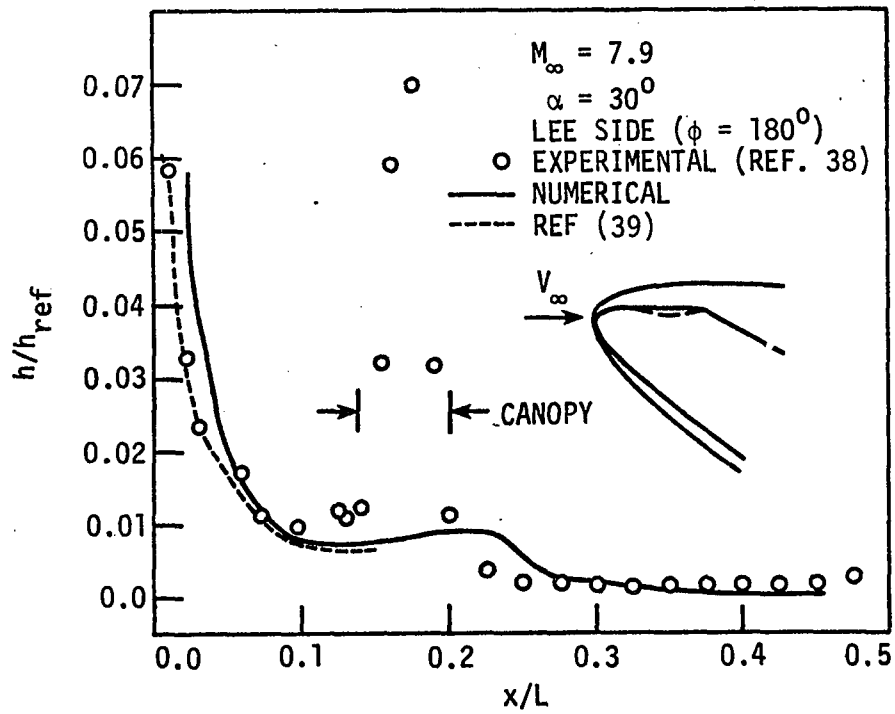Figure 30. Heat transfer comparison on wind side

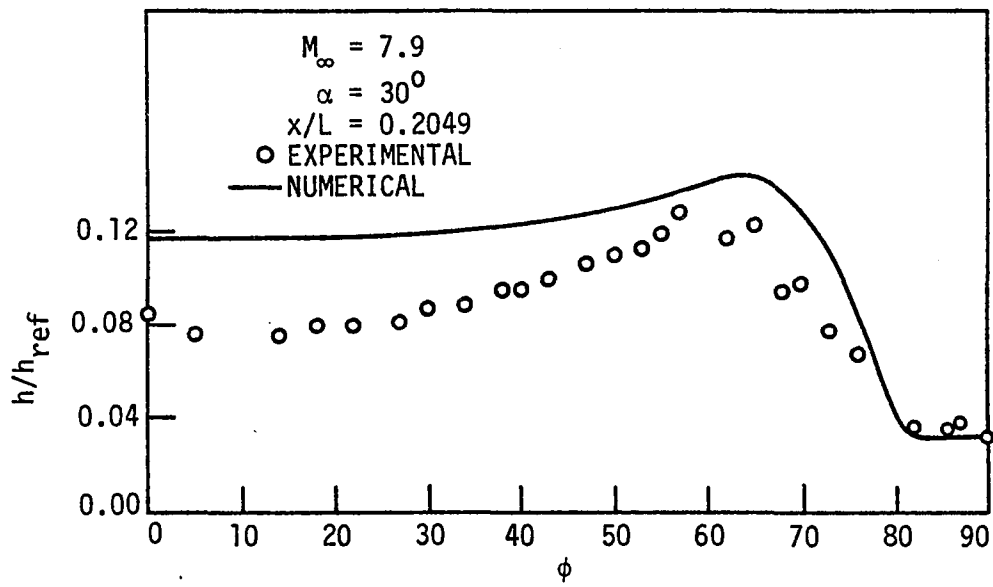Figure 31. Heat transfer comparison on lee side

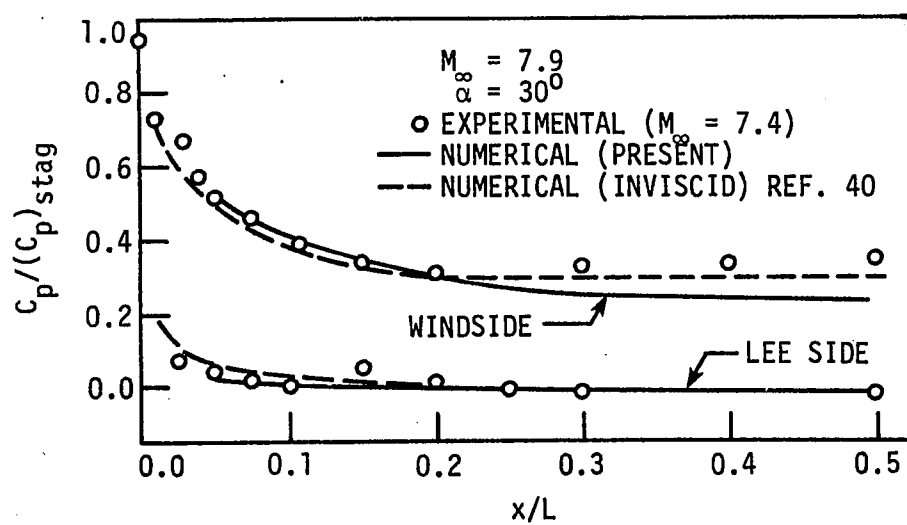Figure 32. Heat transfer comparison at x/L = 0.205

Figure 33. Wall pressure comparison

are C. P. Li's (40) inviscid flow computations at M_∞ = 7.9. Note that the experiment does not resolve the lee side pressure coefficients in the canopy region very well. Figure 34 compares the computed pressure coefficients at x/L = 0.20 with the experimental results and the agreement is very good. The crossflow velocity vector directions at different axial locations are shown in Figures 35, 36, 37, 38 and 39. These figures show the development of the two vortices, one on the lee side and the other near the wing body juncture. The experimental oil flow studies indicate the reattachment point at x/L = 0.48 to be close to the location predicted by the present computations. The local grid structure may play a very important role in resolving the vortex structure in that region. Figure 40 shows the pressure contours; Figure 41 shows the grid structure; and Figure 42 shows the Mach contours all at x/L = 0.35.

The present results were also obtained on a CDC 7600 computer. The generalized PNS code required 1.8 x 10^{-3} seconds per grid point per step for this case. A typical PNS solution at 30 degrees angle of attack took around 400 steps and twenty minutes. The blunt body code, on the other hand, required 3.5 hours of CPU time to converge the solution in the blunt nose region.
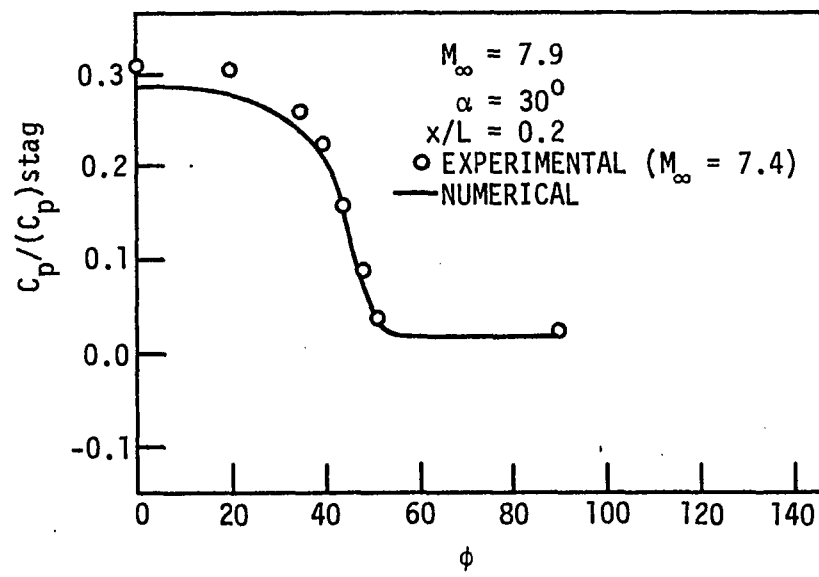
Figure 34. Wall pressure comparison at x/L = 0.2

$$M_\infty = 7.9$$
$$\alpha = 30^0$$
$$x/L = 0.26$$
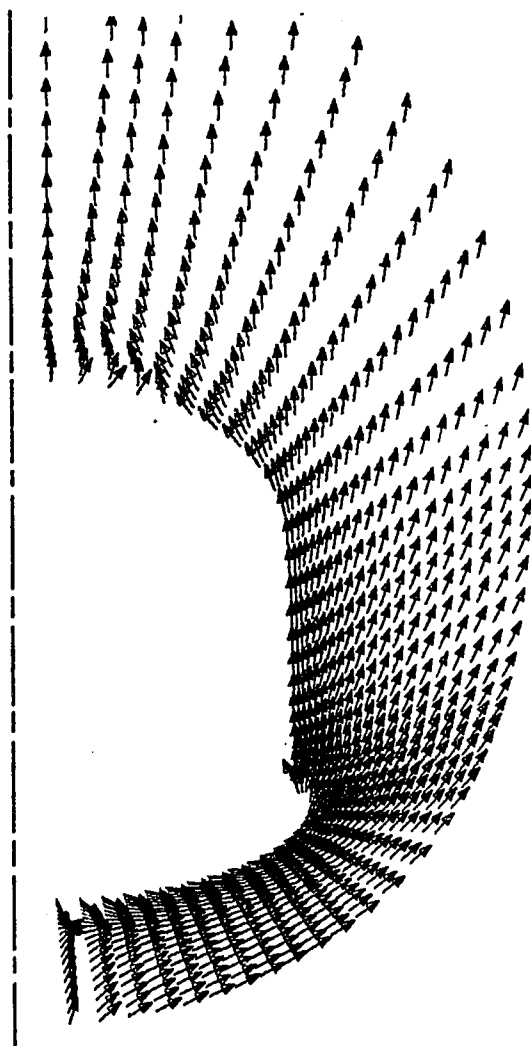
Figure 35. Crossflow velocity vector directions at x/L = 0.26

$$M_\infty = 7.9$$
$$\alpha = 30^0$$
$$x/L = 0.28$$
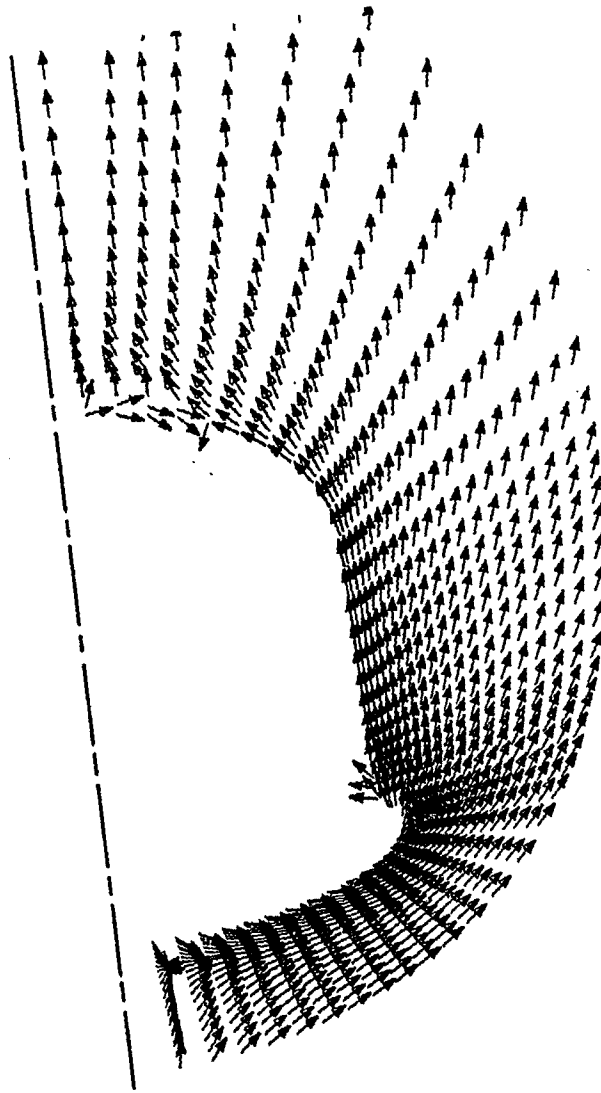
Figure 36. Crossflow velocity vector directions at $x/L = 0.28$

$$M_\infty = 7.9$$
$$\alpha = 30^0$$
$$x/L = 0.30$$
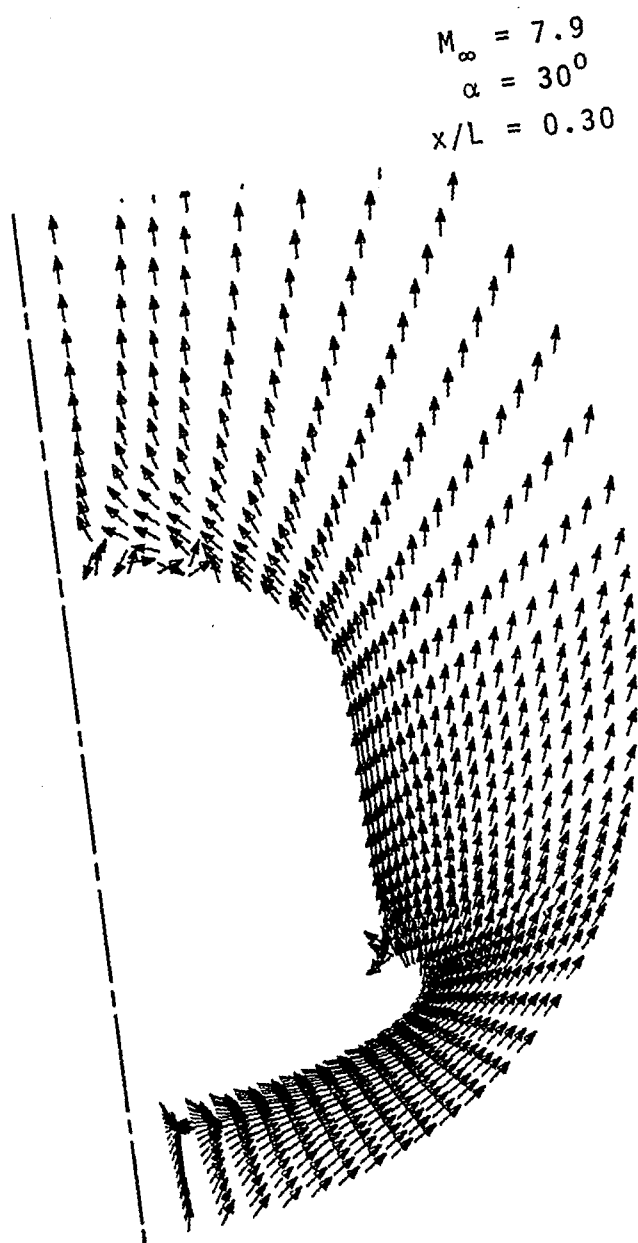
Figure 37. Crossflow velocity vector directions at x/L = 0.30

$$M_\infty = 7.9$$
$$\alpha = 30^0$$
$$x/L = 0.32$$
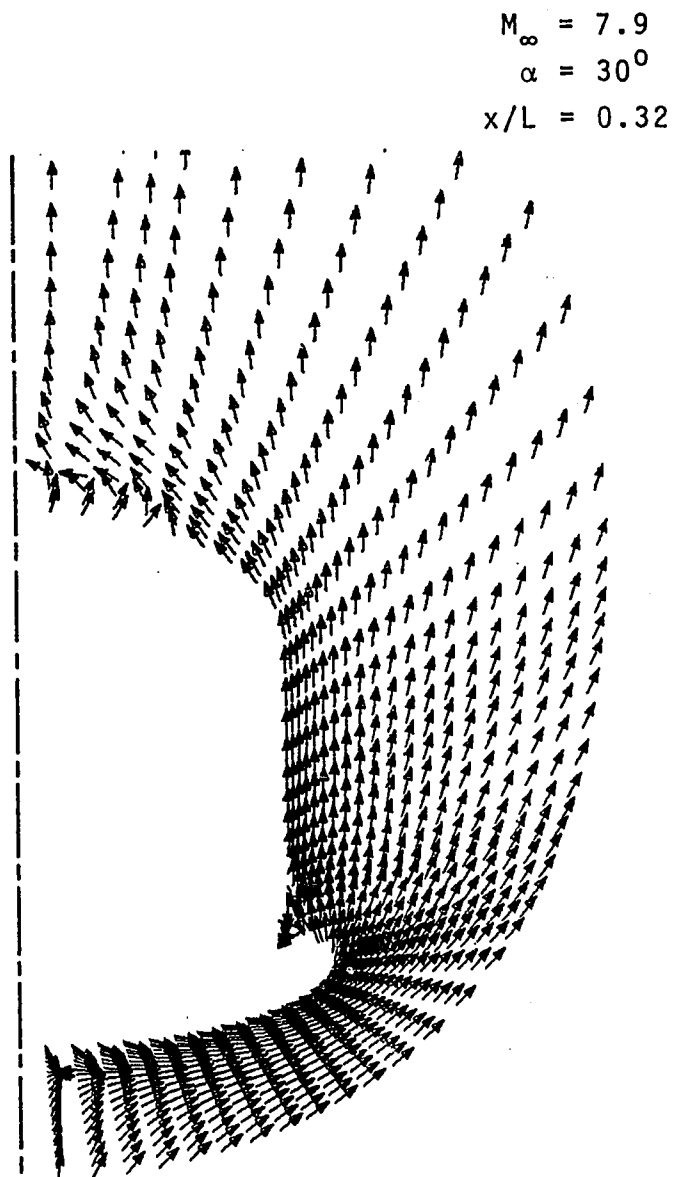
Figure 38. Crossflow velocity vector directions at x/L = 0.32

$$M_\infty = 7.9$$
$$\alpha = 30^\circ$$
$$x/L = 0.48$$

R_3

R_2

R_1
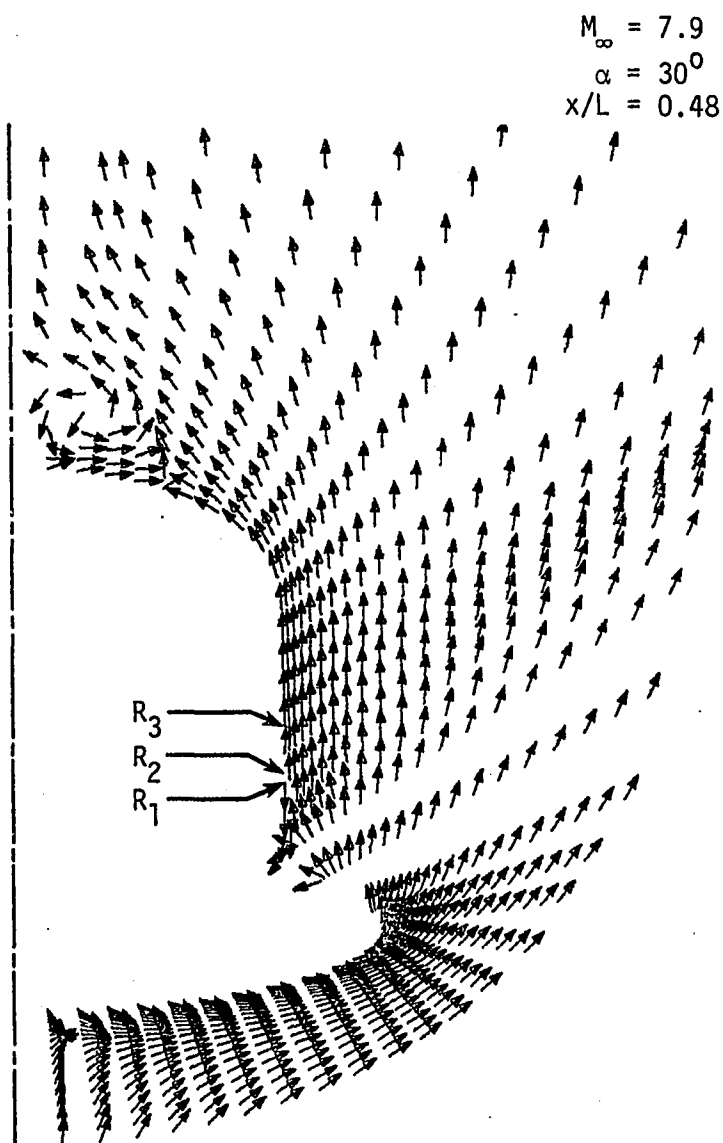
R_1 - EXPERIMENTAL REATTACHMENT POINT
$M_\infty = 5.26$, $\alpha = 20^\circ$

R_2 - COMPUTATIONAL REATTACHMENT POINT
$M_\infty = 7.9$, $\alpha = 30^\circ$

R_3 - EXPERIMENTAL REATTACHMENT POINT
$M_\infty = 5.26$, $\alpha = 40^\circ$

Figure 39. Crossflow velocity vector directions at x/L = 0.48

$M_\infty = 7.9$
$\alpha = 30^0$
$x/L = 0.35$
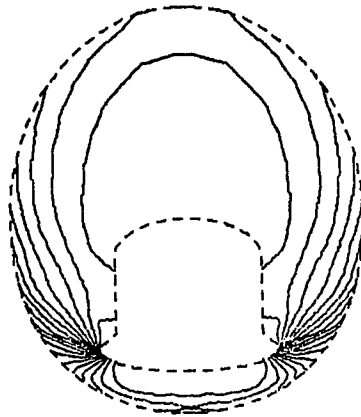
Figure 40. Pressure contours at x/L = 0.35

M_∞ = 7.9
α = 30°
x/L= 0.35
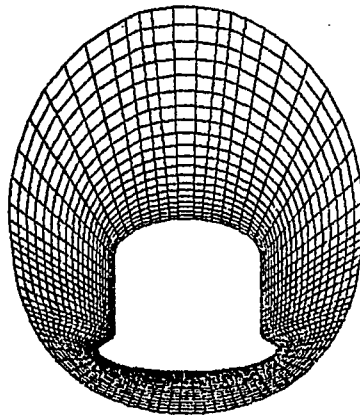
Figure 41.   The grid at x/L = 0.35

$$M_\infty = 7.9$$
$$\alpha = 30^\circ$$
$$x/L = 0.35$$
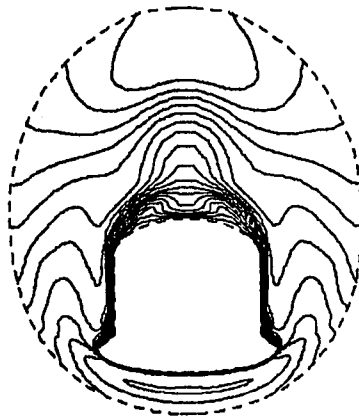
Figure 42. Mach number contours at x/L = 0.35

VII. CONCLUDING REMARKS

A generalized PNS code has been developed to compute the steady viscous supersonic flow around arbitrary body shapes. The code was used to calculate the flow around a slab delta wing at angles of attack up to 41.5° and Mach numbers of 6.8 and 9.6. In addition, the laminar flow around the Space Shuttle Orbiter forebody was computed at 0° and 30° angle of attack and at Mach numbers of 4.6 and 7.9, respectively. The numerical results, including shock shapes, heat transfer coefficients, and pressure coefficients compared well with the experimental results, in all cases. A substantial reduction in computer time was achieved for the Space Shuttle Orbiter forebody flow field calculations because of the generalized marching procedure. It is believed that the use of additional grid points in conjunction with an improved grid generation scheme will improve the solution and allow the marching to proceed well into the aft region of the Space Shuttle Orbiter body.

VIII. REFERENCES

1. Rubin, S. G., and Lin, T. C. "Numerical Methods for Two- and Three-Dimensional Viscous Flow Problems: Application to Hypersonic Leading Edge Equations." PIBAL Rept. No. 71-8. Polytechnic Institute of Brooklyn, Farmingdale, N.Y., April 1971.

2. Lin, T. C., and Rubin, S. G. "Viscous Flow over a Cone at Moderate Incidence: I. Hypersonic Tip Region." Computers and Fluids, 1 (Feb. 1973), 37-57.

3. Lubard, S. C., and Helliwell, W. S. "Calculation of the Flow on a Cone at High Angle of Attack." AIAA Journal, 12 (July 1974), 965-974.

4. Lubard, S. C., and Rakich, J. V. "Calculation of the Flow on a Blunted Cone at a High Angle of Attack." AIAA Paper 75-149, Jan. 1975.

5. Rakich, J. V., and Lubard, S. C. "Numerical Computation of Viscous Flows on the Lee Side of Blunt Shapes Flying at Supersonic Speeds." Proceedings NASA Conference on Aerodynamic Analyses Requiring Advanced Computers, Hampton, Va., March 1975. Also NASA SP-347, NASA.

6. Vigneron, Y. C., Rakich, J. V., and Tannehill, J. C. "Calculation of Supersonic Viscous Flow over Delta Wings with Sharp Subsonic Leading Edges." AIAA Paper 78-1137, July 1978.

7. Schiff, L. B., and Steger, J. L. "Numerical Stimulation of Steady Supersonic Viscous Flow." AIAA Paper 79-0130, Jan. 1979.

8. Tannehill, J. C., Venkatapathy, E., and Rakich, J. V. "Numerical Solution of Supersonic Viscous Flow over Blunt Delta Wings." AIAA Paper 81-0049, Jan. 1981.

9. Rakich, J. V., and Kutler, P. "Comparison of Characteristics and Shock Capturing Methods with Application to the Space Shuttle Vehicle." AIAA Paper 72-191, Jan. 1972.

10. Kutler, P., Lomax, H., and Warming, R. F. "Computation of Space Shuttle Flow Fields Using Noncentered Finite-Difference Schemes." AIAA Journal, 11 (Feb. 1973), 196-204.

11. Moretti, G., Grossman, B., and Marconi, F. Jr. "A Complete Numerical Technique for the Calculation of the Three-Dimensional Inviscid Supersonic Flows." AIAA Paper 72-192, Jan. 1972.

12. Marconi, F., and Salas, M. "Computation of Three Dimensional Flows about Aircraft Configurations." Computers and Fluids, 1 (1973), 185-195.

13. Marconi, F., Yaeger, L., and Hamilton, H. H. "Computation of High Speed Inviscid Flows about Real Configurations." NASA SP-347, 1975, pp. 1411-1455.

14. Chaussee, D. S., Kutler, P., and Holst, T. "Inviscid Supersonic/ Hypersonic Body Flowfield and Aerodynamics from Shock-Capturing Technique Calculations." Journal of Spacecraft and Rockets, 13, No. 6 (June 1976), 325-331.

15. Rakich, J. V., and Lanfranco, H. J. "Numerical Computation of Space Shuttle Laminar Heating and Surface Streamlines." Journal of Spacecraft and Rockets, 14, No. 5 (May 1977), 265-272.

16. Goodrich, W. D., Li, C. P., Houston, C. K., Chiu, P., and Olmedo, L. "Numerical Computations of Orbiter Flow Fields and Laminar Heating Rates." Journal of Spacecraft and Rockets, 14 (May 1977), 257-264.

17. Li, C. P. "Application of an Implicit Technique to the Shock-Layer Flow around General Bodies." AIAA Paper 81-0191, Jan. 1981.

18. Chaussee, D. S., Patterson, J. L., Kutler, P., Pulliam, T. H., and Steger, J. L. "A Numerical Simulation of Hypersonic Viscous Flows over Arbitrary Geometries at High Angle of Attack." AIAA Paper 81-0050, Jan. 1981.

19. Viviand, H. "Conservative Forms of Gas Dynamic Equations." La Recherche Aérospatiale, No. 1, Jan.-Feb. 1974.

20. Lighthill, M. J. "On Boundary Layers and Upstream Influence. II. Supersonic Flows without Separation." Proceedings Roy. Soc. Aero., 217 (1953).

21. Lin, T. C., and Rubin, S. G. "A Numerical Model for Supersonic Viscous Flow over a Slender Reentry Vehicle." AIAA Paper 79-0130, New Orleans, La., Jan. 1979.

22. Helliwell, W. S., and Lubard, S. C. "An Implicit Method for Three-Dimensional Viscous Flow with Application to Cones at Angle of Attack." Computers and Fluids, 3 (1975), 83-101.

23. Helliwell, W. S., Dickinson, R. P., and Lubard, S. C. "Viscous Flow over Arbitrary Geometries at High Angle of Attack." AIAA Paper 80-0064, Pasadena, Calif., Jan. 1980.

24. Lindemuth, I., and Killeen, J. "Alternating Direction Implicit Techniques for Two Dimensional Magnetohydrodynamics Calculations."

Journal of Computational Physics, 13 (Oct. 1973), 181-208.

25. McDonald, H., and Briley, W. R. "Three-Dimensional Supersonic Flow of a Viscous or Inviscid Gas." Journal of Computational Physics, 19 (1975), 150-178.

26. Beam, R., and Warming, R. F. "An Implicit Factored Scheme for the Compressible Navier-Stokes Equations." AIAA Journal, 16 (April 1978), 393-401.

27. Steger, J. L. "Implicit Finite-Difference Simulation of Flow about Arbitrary Geometries with Application to Airfoils." AIAA Paper 77-665, June 1977.

28. Thomas, P. D., Vinokur, M., Bastianon, R. A., and Conti, R. J. "Numerical Solution for Three-Dimensional Inviscid Supersonic Flows." AIAA Journal, 10 (July 1972), 887-894.

29. Bertram, M. H., and Everhart, P. E. "An Experimental Study of the Pressure and Heat Transfer Distribution on a 70° Sweep Slab Delta Wing in Hypersonic Flow." NASA, TR R-153, Dec. 1963.

30. Tannehill, J. C., Holst, T. L., and Rakich, J. V. "Numerical Computation of Two-Dimensional Viscous Blunt Body Flows with an Impinging Shock." AIAA Journal, 4 (Feb. 1976), 204-211.

31. Kutler, P., Reinhardt, W. A., and Warming, R. F. "Numerical Computation of Multishocked Three-Dimensional Supersonic Flow Fields with Real Gas Effects." AIAA Paper 72-702, June 1972.

32. Myers, R. M. "Users Guide for a Three-Dimensional Aircraft Body Fit Program." Technical Memorandum 5060, Lockheed Electronics Company, Houston, 1975.

33. Kutler, P., Pedelty, J. A., and Pulliam, T. H. "Supersonic Flow over Three-Dimensional Ablated Nosetips Using an Unsteady Implicit Numerical Procedure." AIAA Paper 80-0063, Jan. 1980.

34. Rizk, Y. M., Chaussee, D. S., and McRae, D. S. "Computation of Hypersonic Viscous Flow around Three-Dimensional Bodies at High Angles of Attack." AIAA Paper 81-1261, June 1981.

35. Rizzi, A., and Bailey, H. "Reacting Nonequilibrium Flow around the Space Shuttle Using a Time Split Method." NASA SP-347, 1975.

36. Kingsland, R. B. "Aeroheating (Pressure) Characteristics on a 0.010-Scale Version of the Vehicle 3 Space Shuttle Configuration." NASA CR-144608, Vol. 1, May 1976 (IH4).

37. Dye, W. H., and Polek, T. "Results of Pressure Distribution Tests of a 0.01-Scale Space Shuttle Orbiter Model in the NASA/ARC 3.5

Foot Hypersonic Wind Tunnel (Test OH38)." NASA CR-144584, Dec. 1975.

38. Dye, W. H. "Aerodynamic Heating Results Obtained during Test OH50B Conducted in the AEDC VKF Tunnel B Using the 0.040-Scale Model 83-0 of the Space Shuttle Orbiter Forward Fifty Percent Fuselage." NASA CR-151067, June 1977.

39. Lanfranco, J. M. "Critical Evaluation of a Method for Space Shuttle Heat Transfer and Surface Streamline Predictions." Informatics-PMI, Inc., Report TN-1335-44-1, Oct. 1976.

40. Li, C. P. "Numerical Simulation of Reentry Flow around the Shuttle Orbiter Including Real Gas Effects." Computers in Flow Predictions and Fluid Dynamics Experiments. ASME Winter Annual Meeting, Nov. 1981, pp. 141-145.

IX. ACKNOWLEDGMENTS

X. APPENDIX A: DELTA FORM OF THE

FINITE DIFFERENCE ALGORITHM

The PNS equation in conservation law form, given by Eq. (20), is

$$\frac{\partial \overline{E}}{\partial \xi} + \frac{\partial \overline{F}}{\partial \eta} + \frac{\partial \overline{G}}{\partial \zeta} = 0 \tag{A1}$$

Note that

$$\overline{E} = \overline{E}(U, \xi_x, \xi_y, \xi_z)$$

$$\overline{F} = \overline{F}(U, \eta_x, \eta_y, \eta_z) \tag{A2}$$

$$\overline{G} = \overline{G}(U, \zeta_x, \zeta_y, \zeta_z)$$

Define

$$\Delta^i \overline{E} = \overline{E}^{i+1} - \overline{E}^i$$

$$\Delta^i \overline{F} = \overline{F}^{i+1} - \overline{F}^i \tag{A3}$$

$$\Delta^i \overline{G} = \overline{G}^{i+1} - \overline{G}^i$$

The above difference quantities will also satisfy the partial differential

Eq. (A1) and they are given by

$$\frac{\partial \Delta^i \overline{E}}{\partial \xi} + \frac{\partial \Delta^i \overline{E}}{\partial \eta} + \frac{\partial \Delta^i \overline{E}}{\partial \zeta} = 0 \tag{A4}$$

If h is defined as the step size,

$$h = \Delta \xi = \xi^{i+1} - \xi^i \tag{A5}$$

then, the linearized expression for $\Delta^i \overline{E}$ is given by

$$\Delta^i \overline{E} = \frac{\theta_1 h}{1 + \theta_2} \frac{\partial \Delta^i \overline{E}}{\partial \xi} + \frac{h}{1 + \theta_2} \frac{\partial^i \overline{E}}{\partial \xi} + \frac{\theta_2}{1 + \theta_2} \Delta^{i-1} \overline{E} \tag{A6}$$

The above expression is second-order accurate if $\theta_1 = 1$ and $\theta_2 = 1/2$,

and it is first-order accurate for $\theta_1 = 1$ and $\theta_2 = 0$ (Euler implicit

from). Substituting $\frac{\partial \Delta^i \overline{E}}{\partial \xi}$ from Eq. (A4) and $\frac{\partial^i \overline{E}}{\partial \xi}$ from Eq. (A1), into

Eq. (A6), we get

$$\Delta^i\overline{E} = \frac{\theta_1 h}{1 + \theta_2} \left[- \frac{\partial \Delta^i\overline{F}}{\partial \eta} - \frac{\partial \Delta^i\overline{G}}{\partial \zeta} \right]$$

$$+ \frac{h}{1 + \theta_2} \left[- \frac{\partial^i\overline{F}}{\partial \eta} - \frac{\partial^i\overline{G}}{\partial \zeta} \right] \tag{A7}$$

$$+ \frac{\theta_2}{1 + \theta_2} \; \Delta^i\overline{E}.$$

Since $\overline{E} = \overline{E}(\overline{U}, \xi_x, \xi_y, \xi_z)$

$$\Delta^i\overline{E} = \left(\frac{\partial \overline{E}}{\partial \overline{U}}\right)^i \Delta^i\overline{U} + \left(\frac{\partial \overline{E}}{\partial \xi_x}\right)^i \Delta^i\xi_x$$

$$+ \left(\frac{\partial \overline{E}}{\partial \xi_y}\right)^i \Delta^i\xi_y + \left(\frac{\partial \overline{E}}{\partial \xi_z}\right)^i \Delta^i\xi_z. \tag{A8}$$

Similarly,

$$\Delta^i\overline{F} = \left(\frac{\partial \overline{F}}{\partial \overline{U}}\right)^i \Delta^i\overline{U} + \left(\frac{\partial \overline{F}}{\partial \eta_x}\right)^i \Delta^i\eta_x + \left(\frac{\partial \overline{F}}{\partial \eta_y}\right)^i \Delta^i\eta_y$$

$$+ \left(\frac{\partial \overline{F}}{\partial \eta_z}\right)^i \Delta\eta_z \tag{A9}$$

and

$$\Delta^i\overline{G} = \left(\frac{\partial \overline{G}}{\partial \overline{U}}\right)^i \Delta^i\overline{U} + \left(\frac{\partial \overline{G}}{\partial \zeta_x}\right)^i \Delta^i\zeta_x + \left(\frac{\partial \overline{G}}{\partial \zeta_y}\right)^i \Delta^i\zeta_y$$

$$+ \left(\frac{\partial \overline{G}}{\partial \zeta_z}\right)^i \Delta^i\zeta_z. \tag{A10}$$

Substituting Eq. (A8), Eq. (A9) and Eq. (A10) into Eq. (A7), yields

$$\left(\frac{\partial \overline{E}}{\partial \overline{U}}\right)^i \Delta^i\overline{U} + \frac{\theta_1 h}{1 + \theta_2} \left[\frac{\partial}{\partial \eta} \left(\frac{\partial \overline{F}}{\partial \overline{U}}\right)^i \Delta^i\overline{U} + \frac{\partial}{\partial \zeta} \left(\frac{\partial \overline{G}}{\partial \overline{U}}\right)^i \Delta^i\overline{U} \right]$$

$$= - \frac{h}{1 + \theta_2} \left[\frac{\partial^i\overline{F}}{\partial \eta} + \frac{\partial^i\overline{G}}{\partial \zeta} \right] + \frac{\theta_2}{1 + \theta_2} \left[\Delta^{i-1}\overline{E} \right]$$

$$- \left[\left(\frac{\partial \overline{E}}{\partial \xi_x}\right)^i \Delta^i\xi_x + \left(\frac{\partial \overline{E}}{\partial \xi_y}\right)^i \Delta^i\xi_y + \left(\frac{\partial \overline{E}}{\partial \xi_z}\right)^i \Delta^i\xi_z \right]$$

$$- \frac{\theta_1 h}{1 + \theta_2} \left[\frac{\partial}{\partial \eta} \left\{ \left(\frac{\partial \overline{F}}{\partial \eta_x} \right)^i \Delta^i n_x + \left(\frac{\partial \overline{F}}{\partial \eta_y} \right)^i \Delta^i n_y + \left(\frac{\partial \overline{F}}{\partial \eta_z} \right)^i \Delta^i n_z \right\} \right]$$

$$- \frac{\theta_1 h}{1 + \theta_2} \left[\frac{\partial}{\partial \zeta} \left\{ \left(\frac{\partial \overline{G}}{\partial \zeta_x} \right)^i \Delta^i \zeta_x + \left(\frac{\partial \overline{G}}{\partial \zeta_y} \right)^i \Delta^i \zeta_y + \left(\frac{\partial \overline{G}}{\partial \zeta_z} \right)^i \Delta^i \zeta_z \right\} \right]$$

(A11)

By adding the following second order term $[0(\Delta \xi)^2]$ to the LHS of Eq. (A11),

$$\frac{\theta_1 h^2}{1 + \theta_2} \frac{\partial}{\partial \zeta} \left(\frac{\partial \overline{G}}{\partial \overline{U}} \right)^i \left[\left(\frac{\partial \overline{E}}{\partial \overline{U}} \right)^{-1} \right] \frac{\partial}{\partial \eta} \left(\frac{\partial \overline{F}}{\partial \overline{U}} \right) \Delta^i \overline{U}$$

(A12)

the LHS of Eq. (A11) becomes

$$\text{LHS[Eq. A11]} + 0(\Delta \xi^2)$$

$$= \left(\frac{\partial \overline{E}}{\partial \overline{U}} \right)^i \Delta^i \overline{U} + \frac{\theta_1 h}{1 + \theta_2} \frac{\partial}{\partial \eta} \left(\frac{\partial \overline{F}}{\partial \overline{U}} \right)^i \Delta^i \overline{U} + \frac{\theta_1 h}{1 + \theta_2} \frac{\partial}{\partial \zeta} \left(\frac{\partial \overline{G}}{\partial \overline{U}} \right)^i \Delta^i \overline{U}$$

$$+ \frac{\theta_1 h^2}{1 + \theta_2} \frac{\partial}{\partial \zeta} \left(\frac{\partial \overline{G}}{\partial \overline{U}} \right)^i \left[\left(\frac{\partial \overline{E}}{\partial \overline{U}} \right)^{-1} \right] \frac{\partial}{\partial \eta} \left(\frac{\partial \overline{F}}{\partial \overline{U}} \right) \Delta^i \overline{U}$$

(A13)

$$= \left[\left(\frac{\partial \overline{E}}{\partial \overline{U}} \right)^i + \frac{\theta_1 h}{1 + \theta_2} \frac{\partial}{\partial \zeta} \left(\frac{\partial \overline{G}}{\partial \overline{U}} \right)^i \right] \left[I + \frac{\theta_1 h}{1 + \theta_2} \left(\frac{\partial \overline{E}}{\partial \overline{U}} \right)^i \frac{\partial}{\partial \eta} \left(\frac{\partial \overline{F}}{\partial \overline{U}} \right)^i \right] \Delta^i \overline{U}$$

(A14)

$$= \left[\left(\frac{\partial \overline{E}}{\partial \overline{U}} \right)^i + \frac{\theta_1 h}{1 + \theta_2} \frac{\partial}{\partial \zeta} \left(\frac{\partial \overline{G}}{\partial \overline{U}} \right)^i \right] \left(\frac{\partial \overline{E}}{\partial \overline{U}} \right)^{-1} \left[\left(\frac{\partial \overline{E}}{\partial \overline{U}} \right)^i + \frac{\theta_1 h}{1 + \theta_2} \frac{\partial}{\partial \eta} \left(\frac{\partial \overline{F}}{\partial \overline{U}} \right)^i \right] \Delta^i \overline{U}$$

(A15)

The third, fourth and fifth terms on the RHS of Eq. (A11) can be further simplified. Since,

$$\overline{E} = \overline{E}(\overline{U}, \xi_x, \xi_y, \xi_z)$$

$$\left(\frac{\partial \overline{E}}{\partial \xi_x}\right) = \overline{E} = E/J$$

$$\left(\frac{\partial \overline{E}}{\partial \xi_y}\right) = \overline{F} = F/J \qquad\qquad (A16)$$

$$\left(\frac{\partial \overline{E}}{\partial \xi_z}\right) = \overline{G} = G/J$$

Similarly,

$$\frac{\partial \overline{G}}{\partial \zeta_x} = \frac{\partial \overline{F}}{\partial \eta_x} = (\overline{E} - \overline{E}_v) = \frac{E - E_v}{J}$$

$$\frac{\partial \overline{G}}{\partial \zeta_y} = \frac{\partial \overline{F}}{\partial \eta_y} = (\overline{F} - \overline{F}_v) = \frac{F - F_v}{J} \qquad\qquad (A17)$$

$$\frac{\partial \overline{G}}{\partial \zeta_z} = \frac{\partial \overline{F}}{\partial \eta_z} = (\overline{G} - \overline{G}_v) = \frac{G - G_v}{J}$$

Also,

$$\Delta^i \xi_x = \frac{\partial \xi_x}{\partial \xi} \cdot \Delta \xi$$

$$\Delta^i \xi_y = \frac{\partial \xi_y}{\partial \xi} \cdot \Delta \xi$$

$$\Delta^i \xi_z = \frac{\partial \xi_z}{\partial \xi} \cdot \Delta \xi$$

$$\Delta^i \eta_x = \frac{\partial \eta_x}{\partial \xi} \cdot \Delta \xi$$

$$\Delta^i \eta_y = \frac{\partial \eta_y}{\partial \xi} \cdot \Delta \xi \qquad\qquad (A18)$$

$$\Delta^i \eta_z = \frac{\partial \eta_z}{\partial \xi} \cdot \Delta \xi$$

$$\Delta^i \zeta_x = \frac{\partial \zeta_x}{\partial \xi} \cdot \Delta \xi$$

$$\Delta^i \zeta_y = \frac{\partial \zeta_y}{\partial \xi} \cdot \Delta \xi$$

$$\Delta^i \zeta_z = \frac{\partial \zeta_z}{\partial \xi} \cdot \Delta \xi$$

Substituting Eqs. (A16), (A17), and (A18) into the RHS of Eq. (A11) yields,

RHS[Eq. (A11)] =

$$
-\frac{h}{1+\theta_2}\left(\frac{\partial\overline{F}}{\partial\eta}+\frac{\partial\overline{G}}{\partial\zeta}\right)^i +\frac{\theta_2}{1+\theta_2}\;\Delta^{i-1}\overline{E}
$$

$$
-h\left[\left(\frac{\overline{E}}{J}\right)\frac{\partial\xi_x}{\partial\xi}+\left(\frac{F}{J}\right)\frac{\partial\xi_y}{\partial\xi}+\left(\frac{\overline{G}}{J}\right)\frac{\partial\xi_z}{\partial\xi}\right]
$$

$$
-\frac{\theta_1}{1+\theta_2}h^2\left[\frac{\partial}{\partial\eta}\left\{\left(\frac{E-E_v}{J}\right)\frac{\partial\eta_x}{\partial\xi}+\frac{(F-F_v)}{J}\frac{\partial\eta_y}{\partial\xi}\right.\right.
$$

$$
\left.\left.+\left(\frac{G-G_v}{J}\right)\frac{\partial\eta_z}{\partial\xi}\right\}\right]
$$

$$
-\frac{\theta_1}{1+\theta_2}h^2\left[\frac{\partial}{\partial\zeta}\left\{\frac{(E-E_v)}{J}\frac{\partial\zeta_x}{\partial\xi}+\frac{(F-F_v)}{J}\frac{\partial\zeta_y}{\partial\xi}\right.\right.
$$

$$
\left.\left.+\frac{(G-G_v)}{J}\frac{\partial\zeta_z}{\partial\xi}\right\}\right] \tag{A19}
$$

If Vigneron's pressure approximation is made, then

$$
\overline{E}^* = \overline{E} + \overline{P}
$$

This change would add the term $(-\Delta^i\overline{P})$ to the RHS of Eq. (A11) and the form $\frac{\partial\overline{E}}{\partial\overline{U}}$ will be replaced by $\left(\frac{\partial\overline{E}^*}{\partial\overline{U}}\right)$.

With the above changes, Eq. (A15), which represents the LHS of Eq. (A11) and Eq. (A19) which represents the RHS of Eq. (A11) will become,

$$\left[\left(\frac{\partial \overline{E}^*}{\partial \overline{U}}\right) + \frac{\theta_1 h}{1+\theta_2} \frac{\partial}{\partial \zeta}\left(\frac{\partial \overline{G}}{\partial \overline{U}}\right)\right] \left(\frac{\partial \overline{E}^*}{\partial \overline{U}}\right)^{-1} \left[\left(\frac{\partial \overline{E}^*}{\partial \overline{U}}\right) + \frac{\theta_1 h}{1+\theta_2} \frac{\partial}{\partial \eta}\left(\frac{\partial \overline{F}}{\partial \overline{U}}\right)^i\right] \Delta^i \overline{U}$$

$$= -\frac{h}{1+\theta_2}\left(\frac{\partial \overline{F}}{\partial \eta} + \frac{\partial \overline{G}}{\partial \zeta}\right)^i + \frac{\theta_2}{1+\theta_2} \Delta^{i-1}\overline{E} - \Delta^i\overline{P}$$

$$- h\left(\frac{\partial \overline{E}^*}{\partial \xi}\right)^i_{\overline{U}} - \frac{\theta_1 h^2}{1+\theta_2}\left[\frac{\partial}{\partial \eta}\left(\frac{\partial \overline{F}}{\partial \xi}\right)^i_{\overline{U}} + \frac{\partial}{\partial \zeta}\left(\frac{\partial \overline{G}}{\partial \xi}\right)^i_{\overline{U}}\right] \qquad \text{(A20)}$$

The above equation represents the approximate factored scheme as applied to the PNS equations in generalized coordinates.

APPENDIX B: JACOBIANS

The Jacobians $\partial \bar{F}/\partial \bar{U}$ and $\partial \bar{G}/\partial \bar{U}$ are given by

$$\frac{\partial \bar{F}}{\partial \bar{U}} = \frac{\partial}{\partial \bar{U}} \left\{ \frac{1}{J} \left[\eta_x (E-E_v) + \eta_y (F-F_v) + \eta_z (G-G_v) \right] \right\} \tag{B1}$$

$$\frac{\partial \bar{G}}{\partial \bar{U}} = \frac{\partial}{\partial \bar{U}} \left\{ \frac{1}{J} \left[\zeta_x (E-E_v) + \zeta_y (F-F_v) + \zeta_z (G-G_v) \right] \right\} \tag{B2}$$

These Jacobians can be separated into an inviscid part and a viscous part:

$$\frac{\partial \bar{F}}{\partial \bar{U}} = \left(\frac{\partial \bar{F}}{\partial \bar{U}} \right)_{inviscid} - \left(\frac{\partial \bar{F}}{\partial \bar{U}} \right)_{viscous} \qquad \frac{\partial \bar{G}}{\partial \bar{U}} = \left(\frac{\partial \bar{G}}{\partial \bar{U}} \right)_{inviscid} - \left(\frac{\partial \bar{G}}{\partial \bar{U}} \right)_{viscous} \tag{B3}$$
$$\tag{B4}$$

Using the fact that $\bar{U} = U/J$, the inviscid parts of the Jacobians become

$$\left(\frac{\partial \bar{F}}{\partial \bar{U}} \right)_{inviscid} = \eta_x \frac{\partial E}{\partial U} + \eta_y \frac{\partial F}{\partial U} + \eta_z \frac{\partial G}{\partial U} \tag{B5}$$

$$\left(\frac{\partial \bar{G}}{\partial \bar{U}} \right)_{inviscid} = \zeta_x \frac{\partial E}{\partial U} + \zeta_y \frac{\partial F}{\partial U} + \zeta_z \frac{\partial G}{\partial U} \tag{B6}$$

where

$$\frac{\partial E}{\partial U} = \begin{bmatrix} 0 & 1 & 0 & 0 & 0 \\ \frac{\gamma-3}{2}u^2 + \frac{\gamma-1}{2}(v^2+w^2) & (3-\gamma)u & -(\gamma-1)v & -(\gamma-1)w & \gamma-1 \\ -uv & v & u & 0 & 0 \\ -uw & w & 0 & u & 0 \\ [-\gamma e_t + (\gamma-1)(u^2+v^2+w^2)]u & \gamma e_t - (\gamma-1)\frac{3u^2+v^2+w^2}{2} & -(\gamma-1)uv & -(\gamma-1)uw & \gamma u \end{bmatrix} \quad (B7)$$

$$\frac{\partial F}{\partial U} = \begin{bmatrix} 0 & 0 & 1 & 0 & 0 \\ -uv & v & u & 0 & 0 \\ \frac{\gamma-1}{2}(u^2+w^2) + \frac{\gamma-3}{2}v^2 & -(\gamma-1)u & (3-\gamma)v & -(\gamma-1)w & \gamma-1 \\ -vw & 0 & w & v & 0 \\ [-\gamma e_t + (\gamma-1)(u^2+v^2+w^2)]v & -(\gamma-1)uv & \gamma e_t - \frac{\gamma-1}{2}(u^2+3v^2+w^2) & -(\gamma-1)vw & \gamma v \end{bmatrix} \quad (B8)$$

$$\frac{\partial G}{\partial U} = \begin{bmatrix} 0 & 0 & 0 & 1 & 0 \\ -uw & w & 0 & u & 0 \\ -vw & 0 & w & v & 0 \\ \frac{\gamma-1}{2}(u^2+v^2) + \frac{\gamma-3}{2}w^2 & -(\gamma-1)u & -(\gamma-1)v & (3-\gamma)w & \gamma-1 \\ [-\gamma e_t + (\gamma-1)(u^2+v^2+w^2)]w & -(\gamma-1)uw & -(\gamma-1)vw & \gamma e_t - \frac{\gamma-1}{2}(u^2+v^2+3w^2) & \gamma w \end{bmatrix} \quad (B9)$$

The viscous part of $\partial \bar{F}/\partial \bar{U}$ is

$$\left(\frac{\partial \bar{F}}{\partial \bar{U}}\right)_{viscous} = \frac{\partial}{\partial \bar{U}}\left[\frac{1}{J}(\eta_x E_v + \eta_y F_v + \eta_z G_v)\right] \quad (B10)$$

which can be written as

$$\left(\frac{\partial \bar{F}}{\partial \bar{U}}\right)_{viscous} = \frac{\mu}{J\,Re_L}
\begin{bmatrix}
0 & 0 & 0 & 0 & 0 \\[2ex]
-\left[\ell_1\left(\frac{Ju}{\rho}\right)_\eta + \ell_4\left(\frac{Jv}{\rho}\right)_\eta + \ell_5\left(\frac{Jw}{\rho}\right)_\eta\right] & \ell_1\left(\frac{J}{\rho}\right)_\eta & \ell_4\left(\frac{J}{\rho}\right)_\eta & \ell_5\left(\frac{J}{\rho}\right)_\eta & 0 \\[2ex]
-\left[\ell_4\left(\frac{Ju}{\rho}\right)_\eta + \ell_2\left(\frac{Jv}{\rho}\right)_\eta + \ell_6\left(\frac{Jw}{\rho}\right)_\eta\right] & \ell_4\left(\frac{J}{\rho}\right)_\eta & \ell_2\left(\frac{J}{\rho}\right)_\eta & \ell_6\left(\frac{J}{\rho}\right)_\eta & 0 \\[2ex]
-\left[\ell_5\left(\frac{Ju}{\rho}\right)_\eta + \ell_6\left(\frac{Jv}{\rho}\right)_\eta + \ell_3\left(\frac{Jw}{\rho}\right)_\eta\right] & \ell_5\left(\frac{J}{\rho}\right)_\eta & \ell_6\left(\frac{J}{\rho}\right)_\eta & \ell_3\left(\frac{J}{\rho}\right)_\eta & 0 \\[2ex]
\begin{aligned}
& -\ell_1\left(\frac{Ju^2}{\rho}\right)_\eta - \ell_2\left(\frac{Jv^2}{\rho}\right)_\eta \\
& -\ell_3\left(\frac{Jw^2}{\rho}\right)_\eta - 2\ell_4\left(\frac{Juv}{\rho}\right)_\eta \\
& -2\ell_5\left(\frac{Juw}{\rho}\right)_\eta - 2\ell_6\left(\frac{Jvw}{\rho}\right)_\eta \\
& -\ell_7\left\{J\left[\frac{p}{(\gamma-1)\rho^2} - \frac{u^2+v^2+w^2}{2\rho}\right]\right\}_\eta
\end{aligned}
&
\begin{aligned}
& (\ell_1-\ell_7)\left(\frac{Ju}{\rho}\right)_\eta \\
& +\ell_4\left(\frac{Jv}{\rho}\right)_\eta \\
& +\ell_5\left(\frac{Jw}{\rho}\right)_\eta
\end{aligned}
&
\begin{aligned}
& \ell_4\left(\frac{Ju}{\rho}\right)_\eta \\
& +(\ell_2-\ell_7)\left(\frac{Jv}{\rho}\right)_\eta \\
& +\ell_6\left(\frac{Jw}{\rho}\right)_\eta
\end{aligned}
&
\begin{aligned}
& \ell_5\left(\frac{Ju}{\rho}\right)_\eta \\
& +\ell_6\left(\frac{Jv}{\rho}\right)_\eta \\
& +(\ell_3-\ell_7)\left(\frac{Jw}{\rho}\right)_\eta
\end{aligned}
& \ell_7\left(\frac{J}{\rho}\right)_\eta
\end{bmatrix}$$

(B11)

where

$$\ell_1 = \frac{4}{3} \eta_x^2 + \eta_y^2 + \eta_z^2$$

$$\ell_2 = \eta_x^2 + \frac{4}{3} \eta_y^2 + \eta_z^2$$

$$\ell_3 = \eta_x^2 + \eta_y^2 + \frac{4}{3} \eta_z^2$$

$$\ell_4 = \frac{\eta_x \eta_y}{3}$$

$$\ell_5 = \frac{\eta_x \eta_z}{3}$$

$$\ell_6 = \frac{\eta_y \eta_z}{3}$$

$$\ell_7 = \frac{\gamma}{Pr}(\eta_x^2 + \eta_y^2 + \eta_z^2)$$

(B12)

Likewise, the viscous part of $\partial \bar{G}/\partial \bar{U}$ is

$$\left(\frac{\partial \bar{G}}{\partial \bar{U}}\right)_{viscous} = \frac{\partial}{\partial \bar{U}}\left[\frac{1}{J}\left(\zeta_x E_v + \zeta_y F_v + \zeta_z G_v\right)\right]$$

(B13)

which can be written as

$$\left(\frac{\partial \bar{G}}{\partial \bar{U}}\right)_{viscous} = \frac{\mu}{J\,Re_L}
\begin{bmatrix}
0 & 0 & 0 & 0 & 0 \\[2ex]
-\left[m_1\left(\frac{Ju}{\rho}\right)_\zeta + m_4\left(\frac{Jv}{\rho}\right)_\zeta + m_5\left(\frac{Jw}{\rho}\right)_\zeta\right] & m_1\left(\frac{J}{\rho}\right)_\zeta & m_4\left(\frac{J}{\rho}\right)_\zeta & m_5\left(\frac{J}{\rho}\right)_\zeta & 0 \\[2ex]
-\left[m_4\left(\frac{Ju}{\rho}\right)_\zeta + m_2\left(\frac{Jv}{\rho}\right)_\zeta + m_6\left(\frac{Jw}{\rho}\right)_\zeta\right] & m_4\left(\frac{J}{\rho}\right)_\zeta & m_2\left(\frac{J}{\rho}\right)_\zeta & m_6\left(\frac{J}{\rho}\right)_\zeta & 0 \\[2ex]
-\left[m_5\left(\frac{Ju}{\rho}\right)_\zeta + m_6\left(\frac{Jv}{\rho}\right)_\zeta + m_3\left(\frac{Jw}{\rho}\right)_\zeta\right] & m_5\left(\frac{J}{\rho}\right)_\zeta & m_6\left(\frac{J}{\rho}\right)_\zeta & m_3\left(\frac{J}{\rho}\right)_\zeta & 0 \\[2ex]
\begin{aligned}[t]
&- m_1\left(\frac{Ju^2}{\rho}\right)_\zeta - m_2\left(\frac{Jv^2}{\rho}\right)_\zeta \\
&- m_3\left(\frac{Jw^2}{\rho}\right)_\zeta - 2m_4\left(\frac{Juv}{\rho}\right)_\zeta \\
&- 2m_5\left(\frac{Juw}{\rho}\right)_\zeta - 2m_6\left(\frac{Jvw}{\rho}\right)_\zeta \\
&- m_7\left\{J\left[\frac{p}{(\gamma-1)\rho^2} - \frac{u^2+v^2+w^2}{2\rho}\right]\right\}_\zeta
\end{aligned}
&
\begin{aligned}[t]
&(m_1-m_7)\left(\frac{Ju}{\rho}\right)_\zeta \\
&+ m_4\left(\frac{Jv}{\rho}\right)_\zeta \\
&+ m_5\left(\frac{Jw}{\rho}\right)_\zeta
\end{aligned}
&
\begin{aligned}[t]
&m_4\left(\frac{Ju}{\rho}\right)_\zeta \\
&+ (m_2-m_7)\left(\frac{Jv}{\rho}\right)_\zeta \\
&+ m_6\left(\frac{Jw}{\rho}\right)_\zeta
\end{aligned}
&
\begin{aligned}[t]
&m_5\left(\frac{Ju}{\rho}\right)_\zeta \\
&+ m_6\left(\frac{Jv}{\rho}\right)_\zeta \\
&+ (m_3-m_7)\left(\frac{Jw}{\rho}\right)_\zeta
\end{aligned}
& m_7\left(\frac{J}{\rho}\right)_\zeta
\end{bmatrix}$$

where

$$m_1 = \frac{4}{3}\zeta_x^2 + \zeta_y^2 + \zeta_z^2$$

$$m_2 = \zeta_x^2 + \frac{4}{3}\zeta_y^2 + \zeta_z^2$$

$$m_3 = \zeta_x^2 + \zeta_y^2 + \frac{4}{3}\zeta_z^2$$

$$m_4 = \frac{\zeta_x\zeta_y}{3}$$

$$m_5 = \frac{\zeta_x\zeta_z}{3}$$

$$m_6 = \frac{\zeta_y\zeta_z}{3}$$

$$m_7 = \frac{\gamma}{Pr}(\zeta_x^2 + \zeta_y^2 + \zeta_z^2)$$

(B15)

In Eqs. (B11) and (B14), the expression $(\ )_\eta$ is equivalent to $\frac{\partial}{\partial\eta}(\ )$. Also in these equations, the cross derivative viscous terms have been neglected and μ is assumed to depend only on the position and not on the vector U. These assumptions are consistent with the Euler implicit scheme.

The Jacobian $\partial\bar{E}*/\partial\bar{U}$ is .given by

$$\frac{\partial\bar{E}*}{\partial\bar{U}} = \frac{\partial}{\partial\bar{U}}\left[\frac{1}{J}(\xi_x E* + \xi_y F* + \xi_z G*)\right]$$

(B16)

or

$$\frac{\partial\bar{E}*}{\partial\bar{U}} = \xi_x\frac{\partial E*}{\partial U} + \xi_y\frac{\partial F*}{\partial U} + \xi_z\frac{\partial G*}{\partial U}$$

(B17)

The Jacobians $\partial E^*/\partial U$, $\partial F^*/\partial U$ and $\partial G^*/\partial U$ are given below

$$\frac{\partial E^*}{\partial U} = \begin{bmatrix} 0 & 1 & 0 & 0 & 0 \\[2mm] \frac{\omega(\gamma-1)-2}{2}u^2 + \frac{\omega(\gamma-1)}{2}(v^2+w^2) & [2-\omega(\gamma-1)]u & -\omega(\gamma-1)v & -\omega(\gamma-1)w & \omega(\gamma-1) \\[2mm] -uv & v & u & 0 & 0 \\[2mm] -uw & w & 0 & u & 0 \\[2mm] [-\gamma e_t + (\gamma-1)(u^2+v^2+w^2)]u & \gamma e_t - (\gamma-1)\frac{3u^2+v^2+w^2}{2} & -(\gamma-1)uv & -(\gamma-1)uw & \gamma u \end{bmatrix} \tag{B18}$$

$$\frac{\partial F^*}{\partial U} = \begin{bmatrix} 0 & 0 & 1 & 0 & 0 \\[2mm] -uv & v & u & 0 & 0 \\[2mm] \frac{\omega(\gamma-1)-2}{2}v^2 + \frac{\omega(\gamma-1)}{2}(u^2+w^2) & -\omega(\gamma-1)u & [2-\omega(\gamma-1)]v & -\omega(\gamma-1)w & \omega(\gamma-1) \\[2mm] -vw & 0 & w & v & 0 \\[2mm] [-\gamma e_t + (\gamma-1)(u^2+v^2+w^2)]v & -(\gamma-1)uv & \gamma e_t - \frac{(\gamma-1)}{2}(u^2+3v^2+w^2) & -(\gamma-1)vw & \gamma v \end{bmatrix} \tag{B19}$$

$$\frac{\partial G^*}{\partial U} = \begin{bmatrix} 0 & 0 & 0 & 1 & 0 \\[2mm] -uw & w & 0 & u & 0 \\[2mm] -vw & 0 & w & v & 0 \\[2mm] \frac{\omega(\gamma-1)}{2}(u^2+v^2)+\frac{[\omega(\gamma-1)-2]}{2}w^2 & -\omega(\gamma-1)u & -\omega(\gamma-1)v & [2-\omega(\gamma-1)]w & \omega(\gamma-1) \\[2mm] [-\gamma e_t + (\gamma-1)(u^2+v^2+w^2)]w & -(\gamma-1)uw & -(\gamma-1)vw & \gamma e_t - \frac{(\gamma-1)}{2}(u^2+v^2+3w^2) & \gamma w \end{bmatrix} \tag{B20}$$

APPENDIX C: SHOCK FITTING PROCEDURE

The shock standoff distance δ is determined at station i+1 using the Euler formula

$$\delta^{i+1} = \delta^i + \left(\frac{\partial \delta}{\partial \xi}\right)^i \Delta\xi \tag{C1}$$

The shock slope $\partial \delta / \partial \xi$ is given by

$$\delta_\xi = \frac{-A_2 + \sqrt{A_2^2 - 4A_1A_3}}{2A_1} \tag{C2}$$

where

$$A_1 = V_N^2\left(\epsilon_{12}^2 + \epsilon_{22}^2 + \epsilon_{32}^2\right) - \left(\epsilon_{12}^2 u_\infty^2 + \epsilon_{22}^2 v_\infty^2 + \epsilon_{32}^2 w_\infty^2 + 2\epsilon_{12}\epsilon_{22}u_\infty v_\infty\right.$$
$$\left. + 2\epsilon_{22}\epsilon_{32}v_\infty w_\infty + 2\epsilon_{12}\epsilon_{32}u_\infty w_\infty\right) \tag{C3}$$

$$A_2 = V_N^2\left(2\epsilon_{11}\epsilon_{12} + 2\epsilon_{21}\epsilon_{22} + 2\epsilon_{31}\epsilon_{32}\right) - \left[2\epsilon_{11}\epsilon_{12}u_\infty^2 + 2\epsilon_{21}\epsilon_{22}v_\infty^2 + 2\epsilon_{31}\epsilon_{32}w_\infty^2\right.$$
$$\left. + 2\left(\epsilon_{12}\epsilon_{21} + \epsilon_{22}\epsilon_{11}\right)u_\infty v_\infty + 2\left(\epsilon_{21}\epsilon_{32} + \epsilon_{31}\epsilon_{22}\right)v_\infty w_\infty + 2\left(\epsilon_{31}\epsilon_{12} + \epsilon_{11}\epsilon_{32}\right)u_\infty w_\infty\right] \tag{C4}$$

$$A_3 = V_N^2\left(\epsilon_{11}^2 + \epsilon_{21}^2 + \epsilon_{31}^2\right) - \left(\epsilon_{11}^2 u_\infty^2 + \epsilon_{21}^2 v_\infty^2 + \epsilon_{31}^2 w_\infty^2\right.$$
$$\left. + 2\epsilon_{11}\epsilon_{21}u_\infty v_\infty + 2\epsilon_{21}\epsilon_{31}v_\infty w_\infty + 2\epsilon_{11}\epsilon_{31}u_\infty w_\infty\right) \tag{C5}$$

and

$$\epsilon_{11} = \left[(y_b)_\xi + \delta(\vec{n} \cdot \vec{j})_\xi\right]z_\zeta - \left[(z_b)_\xi + \delta(\vec{n} \cdot \vec{k})_\xi\right]y_\zeta$$

$$\epsilon_{12} = (\vec{n} \cdot \vec{j})z_\zeta - (\vec{n} \cdot \vec{k})y_\zeta$$

$$\epsilon_{21} = \left[(z_b)_\xi + \delta(\vec{n} \cdot \vec{k})_\xi\right]x_\zeta - \left[(x_b)_\xi + \delta(\vec{n} \cdot \vec{i})_\xi\right]z_\zeta$$

$$\epsilon_{22} = (\vec{n} \cdot \vec{k})x_\zeta - (\vec{n} \cdot \vec{i})z_\zeta$$

$$\epsilon_{31} = \left[(x_b)_\xi + \delta(\vec{n} \cdot \vec{i})_\xi\right]y_\zeta - \left[(y_b)_\xi + \delta(\vec{n} \cdot \vec{j})_\xi\right]x_\zeta$$

$$\epsilon_{32} = (\vec{n} \cdot \vec{i})y_\zeta - (\vec{n} \cdot \vec{j})x_\zeta$$

(C6)

In the above equations, V_N represents the upstream flow velocity normal to the shock.

Once the new shock position is determined at station i+1, the pressure behind the shock (p_s) can be determined using a one-sided difference at k=NK in the numerical algorithm, Eq. (25). The remaining flow variables are then computed using the exact shock jump relations. For example, the density at the shock (ρ_s) and V_N are given by.

$$\rho_s = \rho_{NK} = \frac{\gamma M_\infty^2 p_s + \left(\frac{\gamma-1}{\gamma+1}\right)}{1 + \gamma\left(\frac{\gamma-1}{\gamma+1}\right)M_\infty^2 p_s}$$

(C7)

$$V_N = \left\{\frac{\gamma+1}{2\gamma M_\infty^2}\left[\gamma M_\infty^2 p_s + \left(\frac{\gamma-1}{\gamma+1}\right)\right]\right\}^{1/2}$$

(C8)